Journal of Sedimentary Research

Journal of Sedimentary Research, 2013, v. 82, 12–36
Research Article
DOI: 10.2110/jsr.2013.3

SYNDEPOSITIONAL DEFORMATION FEATURES IN HIGH-RELIEF CARBONATE PLATFORMS: LONG-LIVED CONDUITS FOR DIAGENETIC FLUIDS

DAVID A. BUDD,[1] EDMUND L. FROST, III,*[2] KATHARINE W. HUNTINGTON,[3] AND PATRICIA F. ALLWARDT[2]
[1]*Department of Geological Sciences, University of Colorado, Boulder, Colorado 80309, U.S.A.*
[2]*ConocoPhillips Subsurface Technology, 600 North Dairy Ashford, Houston, Texas 77079, U.S.A.*
[3]*Department of Earth and Space Sciences, University of Washington, Seattle, Washington 98195, U.S.A.*
e-mail: budd@colorado.edu

ABSTRACT: **Syndepositional faults and fractures are known to affect early fluid flow in carbonate platforms. Less clear is whether they are active fluid conduits throughout the entire history of the platform strata. Syndeformational fractures in Permian (late Guadalupian) carbonates exposed in Dark Canyon, Guadalupe Mountains, New Mexico, U.S.A., address this question. Transmitted-light and cathodoluminescent petrography, stable-isotope and fluid-inclusion analyses, and clumped-isotope thermometry show that there were multiple episodes of fracturing, dissolution, cementation, and replacement in the fractures. Dolomite cement or dolomitized marine cements line the walls of some fractures and indicate the syndepositional reflux of evaporated Permian seawaters through the fractures. Fine- to medium-crystalline, luminescently zoned calcite may overlie the dolomite and marine cements, line fracture walls where those phases are absent, or cement karst breccia on fracture walls. The $\delta^{18}O$ values of this calcite (−8.8 to −14.0‰ VPDB) and clumped-isotope temperatures (16° to 32°C) indicate precipitation from meteoric fluids ($\delta^{18}O_{SMOW}$ of −6.2 to −10.5‰) associated with episodic sea-level lowstands during the development of high-frequency depositional sequences. The early calcites can themselves be fractured, rotated, and recemented, indicating recurrent deformation and meteoric influx.**

Evaporite cements were once the dominant pore-filling phase in the fractures, forming both before and after the early meteoric cements. The earliest evaporites formed during deposition of Tansill limestone, probably from the same brines that formed dolomites. Evaporites that postdate the early calcite probably did not form until Permo-Triassic burial, when geomechanical analysis indicates that the syndepositional fractures were likely reactivated and brines could have been sourced from overlying bedded evaporite. All evaporite cements subsequently were calcitized, mainly by coarse-crystalline, inclusion-rich calcites that formed from warm (59° to 96°C) fluids. Calculated fluid isotopic compositions ($\delta^{18}O_{SMOW}$ of −0.5 to −4.7‰) imply mixing of meteoric and oil-field brines. Carbon isotope values (+2 to −17‰) indicate microbial degradation of hydrocarbons in some of those fluids, but not all. Geomechanical analysis indicates the potential for syndepositional fractures to have failed (reactivated) during Basin and Range extension, and the warm basinal fluids are interpreted to have migrated upward through the fractures during that event. Platform-margin fractures (unassociated with faults) witnessed cooler fluids (59° to 65°C) than outer-shelf fractures (70° to 96°C) because outer-shelf faults tapped waters from greater depths. The most recent fluid flow through the fractures generated dissolution features and laminated speleogenetic calcites, which are interpreted to result from intrastratal karsting associated with exhumation and weathering.

Diagenetic features in the syndepositional fractures are equivalent to those observed in the adjacent limestones, suggesting active fluid communication between matrix and fractures throughout the diagenetic history of the rocks. The complex fracture paragenesis also indicates that syndepositional fractures are not only conduits for early fluid-flow networks, but they can also impact a rock's entire diagenetic history if reactivated by changing stress fields.

INTRODUCTION

The Guadalupe Mountains in southeastern New Mexico and western Texas, U.S.A., are renowned for their outstanding exposures of Permian carbonate ramps and platforms (Fig. 1). These rocks have been used by successive generations of carbonate geologists to investigate the leading research questions of their day. Most recently, the Guadalupe Mountains have provided outcrop analogs for the study of syndepositional deformation processes and products in the outer-shelf and platform-margin carbonates (Hunt and Fitchen 1999; Hunt et al. 2002; Koša et al. 2003; Stanton and Pray 2004; Koša and Hunt 2005, 2006a; Resor and Flodin 2010; Rush and Kerans 2010; Frost et al. 2012). These efforts have demonstrated that fractures, faults, growth monoclines, and small-scale grabens are common, and affected lateral facies continuity and stratal architecture. The syndepositional fractures and faults also served as

* Present Address: Bureau of Economic Geology, The University of Texas at Austin, Austin, Texas 78713, U.S.A.

Published Online: January 2013
 1527-1404/13/082-012/$03.00

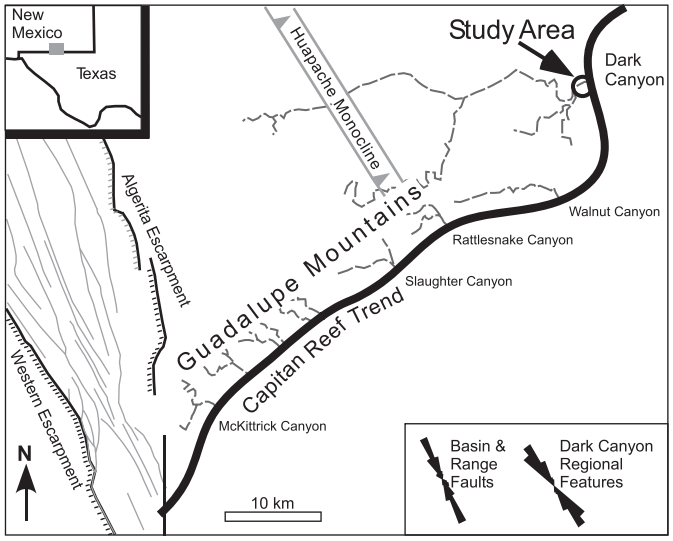

FIG. 1.—Map of the study area showing location of the Dark Canyon outcrop, location of the Capitan reef trend at its terminal position (bold line), various canyons (dashed lines), escarpments (hachured black lines) that expose the Middle to Upper Permian strata, and Basin and Range structural features (gray lines). Inset in upper left shows location of the study area along the Texas–New Mexico state border. Also shown are rose diagrams of Basin and Range-age normal faults along the Western Escarpment and regional syndepositional deformation features documented in Dark Canyon by Frost et al. (2012).

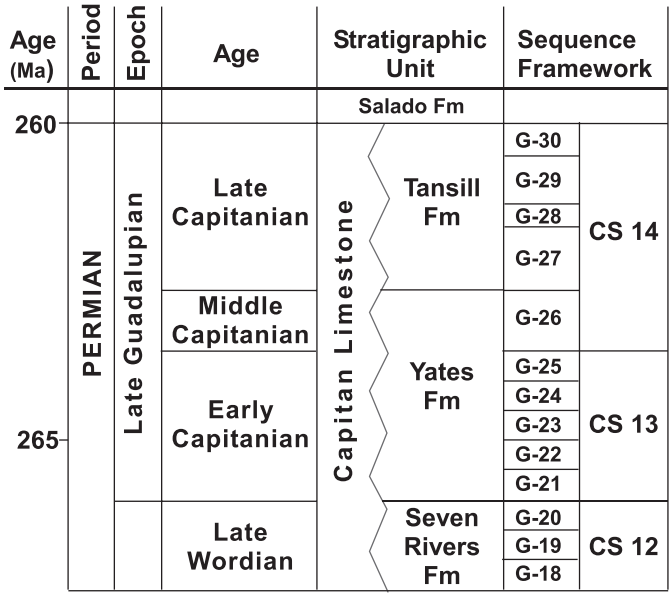

FIG. 2.—Stratigraphic units and the general sequence stratigraphic architecture of late Guadalupian section in Dark Canyon (Fm = Formation). Composite sequences (CS) are from Kerans and Tinker (1999). The youngest composite sequence (CS 14) is in turn composed of five high-frequency sequences known as G-26 through G-30 (from Frost et al. 2012).

conduits that transmitted brines and meteoric fluids deeply into underlying strata and affected early diagenesis, particularly the focusing of karst processes (Hunt et al. 2002; Koša et al. 2003; Koša and Hunt 2006a) and early dolomitization (Melim and Scholle 2002; Hunt et al. 2002; Koša et al. 2003; Frost et al. 2012).

Coarse- to extremely coarse-crystalline calcite spars are the final paragenetic phase in the factures and faults exposed in the Guadalupe Mountains, thus those spars have routinely been interpreted as "late" (e.g., Scholle et al. 1992; Hill 1996; Koša et al. 2003; Stanton and Pray 2004; Koša and Hunt 2006a). But the "late" spars in the fracture fills have not been analyzed in great detail, leaving unresolved questions such as, are there multiple generations of late spar, how "late" is late, and were the syndepositional deformation features active fluid conduits throughout the strata's entire history? This study addresses those questions using a detailed petrographic and isotopic study of the diagenetic features in the syndepositional fracture fills and a geomechanical analysis of regional stress throughout the rocks' history. The results illustrate that the diagenetic history of the syndepositional deformation features provides insight into postdepositional fluid flow through those features and the burial diagenesis of the outer-shelf and platform margin.

STUDY AREA

The Permian carbonate platform strata of the Guadalupe Mountains include fourteen composite sequences (CS), beginning with the Leonardian Clear Fork Formation and culminating with the late Guadalupian Tansill Formation (Kerans and Fitchen 1995; Kerans and Tinker 1999). The Tansill Formation (Fig. 2), which is the focus of this study, is CS 14 and contains four high-frequency sequences (HFS), referred to as Guadalupian HFS 27, 28, 29, and 30 (Rush and Kerans 2010; Frost et al. 2012).

During deposition of the Tansill CS, the platform margin was constructed by a consortium of microbial organisms, reef-building metazoans, and copious amounts of marine cement (Babcock 1977; Mazzullo and Cys 1977; Schmidt 1977; Toomey and Cys 1977; Yurewicz 1977; Babcock and Yurewicz 1989; Kirkland et al. 1993, 1999; Wood et al. 1994, 1996; Wood 1999; Weidlich and Fagerstrom 1999). The top of the CS 14 reef formed in relatively shallow water depths (< 13 m; Babcock and Yurewicz 1989; Tinker 1998; Osleger 1998; Kirkland et al. 1999; Kerans and Tinker 1999). Landward of the platform margin is the outer-shelf facies tract, which is dominated by packstones and grainstones. The outer-shelf transitions into foreshore to shoreface grainstone and tepee-pisolite complexes of the shelf-crest facies tract, which is interpreted by many workers to represent a barrier-island complex (Dunham 1972; Esteban and Pray 1977, 1983; Kendall and Warren 1987; Kerans and Harris 1993; Kerans and Tinker 1999; Rush and Kerans 2010). Landward of the shelf crest are the fenestral grain flats, wackestones, mudstones, evaporites, and fine-grained clastics of the inner-shelf facies tract.

Syndepositional deformation in the platform margin reef is characterized by opening-mode fractures, commonly referred to as neptunian dikes, which are chiefly filled with sandstone and/or encrusting carbonate organisms, early marine cements, and skeletal sediment (Dunham 1972; Yurewicz 1977; Melim and Scholle 2002; Stanton and Pray 2004). Sediment-, breccia- and cement-filled fractures, growth faults, and filled paleocaverns developed along fractures and faults in outer-shelf strata (Hunt and Fitchen 1999; Hunt et al. 2002; Koša et al. 2003; Koša and Hunt 2005, 2006a; Rush and Kerans 2010; Frost et al. 2012). Koša et al. (2003) described seven different lithofacies infilling paleocaverns, with all lithofacies related to either karsting or deposition of coeval platform facies.

The Tansill-age (late Guadalupian) outcrop in Dark Canyon, located near the northeast terminus of the Guadalupe Mountains (Fig. 1), was selected for study due to the excellent and accessible outcrops that exhibit syndepositional deformation features. At the base of the north canyon wall, stacked outer-shelf facies of HFS 27 to 29 are exposed (Fig. 3), and are overlain by stacked packages of shelf-crest deposits. The HFS 30 reef facies described by Toomey and Cys (1977) is exposed on the north wall at the mouth of the canyon.

Frost et al. (2012) mapped seven syndepositional faults and ~ 80 syndepositional fractures in the outer-platform facies exposed along base of the north wall (Fig. 4). The deformation features are oriented parallel

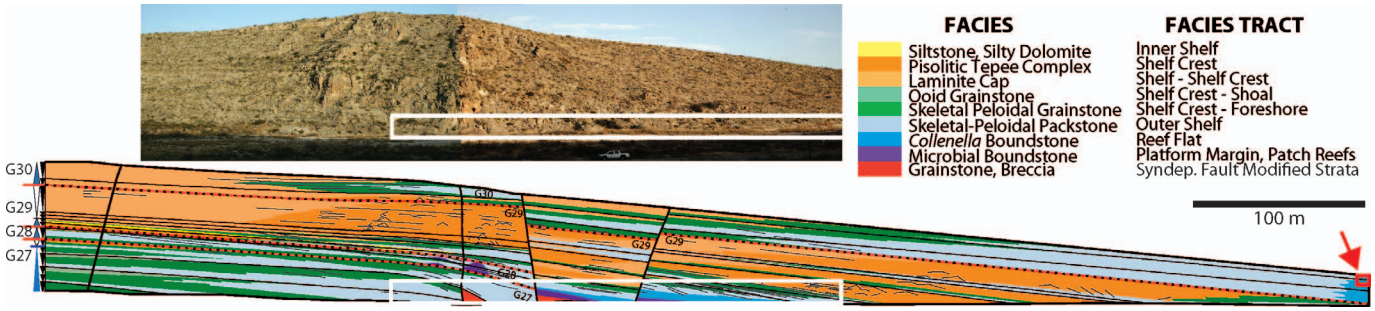

FIG. 3.—Stratigraphic character of the study area. Upper image is a composite photograph of the Dark Canyon outcrop exposure. Lower image shows the distribution of high-frequency sequences (G27 to G30), facies, facies tracts, and syndepositional faults in the Dark Canyon study area (from Frost et al. 2012). In both images, the white box marks the position of the outcrop studied in detail (Fig. 4). Syndepositional fractures were also sampled in the G30 reef facies at the mouth of the canyon (red arrow and box, far right).

to the platform margin with subvertical traces, and they typically crosscut the entire exposed Tansill section. The opening-mode fractures have apertures that range from roughly 0.5 cm to 100 cm, fault displacements range from a few centimeters up to 18 meters, and the faults display growth strata (Frost et al. 2012). Faulting is inferred to have begun during deposition of the underlying Yates Formation, with vertical slip initiating with progressive loading during deposition of Tansill CS14. Fills in the early deformation features in Dark Canyon include both

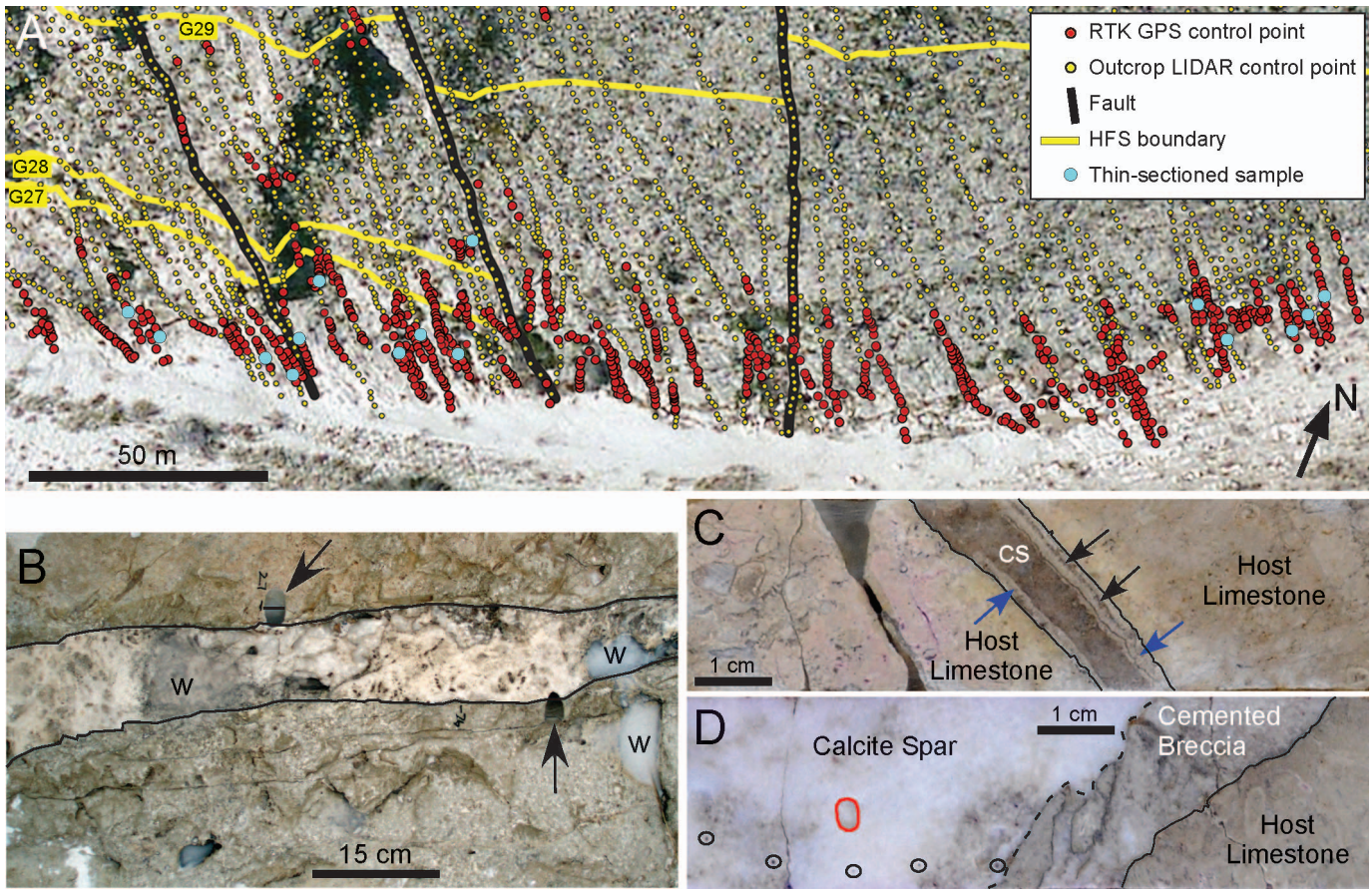

FIG. 4.—Distribution and macroscopic attributes of syndepositional fractures. **A)** Distribution of syndepositional fractures and faults in outer-shelf limestones (from Frost et al. 2012). Each small circle marks a point on a fracture or fault, as determined by real-time kinematic GPS positioning (red circles) or ground-based LIDAR image analysis (yellow circles). Fracture fills thin sectioned are shown by light blue dots. Four additional fills from the G30 HFS at the mouth of the canyon (Fig. 3) were also sectioned. Base image is an airborne LIDAR digital outcrop model of the Dark Canyon study window from Frost et al. (2012). **B)** Outcrop surface showing a calcite-filled syndepositional fracture. Fracture walls are highlighted in black. Arrows point to empty holes of core plugs cut diagonally into the fracture fills. Gray areas (w) are water on the outcrop face. **C)** Slab and polished core plug with fracture walls outlined in black. Walls are lined with an originally fibrous, and now partially dolomitized, isopachous cement (blue arrows) that have calcite cement filling dissolution voids in the isopachous cement (black arrows). Coarse calcite spar (cs) fills center of fracture. **D)** Slab and polished core plug showing fracture wall (black line) overlain by calcite-cemented breccia, which in turn is overlain by coarse-crystalline calcite spar. Small circles denote location of stable-isotope samples; red line outlines a clumped-isotope subsample.

syndepositional and postdepositional components (Frost et al. 2012), suggesting that each feature records multiple diagenetic events. It is the diagenetic fills of the syndepositional deformation features that are the focus of this study.

METHODS

Sampling

Cylindrical samples of 2.5 cm diameter and 7 to 10 cm lengths were drilled from the Dark Canyon outcrops. Thirty-six samples from 26 different syndepositional fractures were collected, with five of those samples taken in the HFS 30 reef facies (far left in Fig. 3) and the remainder from an outcrop window 265 m long in the outer-shelf facies tract (Figs. 3, 4). Seven lateral transects were also drilled through the adjacent strata. The transects were 3.4 to 30.8 m in length, with samples spaced anywhere from 3 cm to ~ 3 m along each transect. Transects generally were begun updip of a syndepositional fault or fracture and extended downdip within the same bed and across deformation features.

Petrographic and Geochemical Analyses

Thin sections were cut from 107 samples of host limestone and 19 samples of fracture fills from 19 different fractures (Fig. 4). Standard transmitted-light microscopy was used to determine the general paragenetic history in each thin section. Cement crystal sizes were described in accordance with Folk (1974; 4 μm < very fine < 16 μm < fine < 62 μm < medium < 250 μm < coarse < 1 mm < very coarse < 4 mm). Epifluorescence microscopy was used to detect hydrocarbon inclusions in diagenetic phases. Cathodoluminescence (CL) microscopy was performed using a Technosyn cold-cathodoluminescence unit (Cambridge Imaging Technology, Ltd) attached to a polarizing microscope. Operating conditions were 12–14 kV, 450–550 μA, and 0.08 torr pressure. Photomicrographs were taken using an Optronics Magnafire™ digital camera (www.optronicsinc.com), which contains a Peltier-cooled image sensor that captures low light intensities and subtle CL patterns.

Fluid-inclusion analyses were performed on eight samples of fracture-fill calcites. Sixteen doubly polished slides of ~ 60 μm thickness were prepared with a low-speed saw and low-temperature curing epoxy to avoid stretching fluid inclusions. Microthermometry measurements were made using a Linkam THMSG 600 heating-cooling stage (www.linkam.co.uk/thmsg600-features/). Homogenization temperatures (T_h) were measured twice by cycling systematically from low to high temperature to avoid stretching of the fluid inclusions. Eutectic temperatures and final ice melting temperatures (Tm) were obtained after T_h measurements and without artificial stretching of the inclusions. Measurement accuracy for T_h and T_m values were ± 1 and ± 0.1°C, respectively. Fluid-inclusion data are available in the Supplemental Data (see Acknowledgments).

Stable-isotope analyses were made on eight dolomites associated with early fractures and on 96 calcite phases. The calcites were microsampled from polished samples and include cements (n = 16) and calcitized evaporite pseudomorphs (n = 16) in host limestones, and cements associated with fracture fills (n = 64). Analyses were performed at the University of Kansas Paleoenvironmental Stable Isotope Laboratory. Twenty to 80 μg of sample were roasted under vacuum at 200°C for an hour to release any volatile organic compounds. Samples were then reacted for 12 minutes under vacuum with three drops of 100% phosphoric acid (r = 1.8913 g/cm^3) at 75°C. Isotopic ratios of the liberated CO_2 gas were measured with a Kiel Carbonate Device III and duel inlet Finnigan MAT253 isotope ratio mass spectrometer with a reported laboratory precision of 0.06‰ for $\delta^{13}C$ and 0.12‰ for $\delta\ ^{18}O$. Stable-isotope results are available in the Supplemental Data (see Acknowledgments).

Seventeen samples of calcite (and four replicates) from seven different syndepositional fracture fills were analyzed for clumped-isotope thermometry (Eiler 2007) at the California Institute of Technology. For each analysis, 8 to 9 mg of calcite was reacted under vacuum at 90°C in 100% phosphoric acid for 10 minutes using an autosampler and common acid bath (Passey et al. 2010). The resultant CO_2 was purified cryogenically multiple times under vacuum and by passage through a Poropak-Q gas chromatograph column held at −20°C while entrained in He (25 mL/min flow rate). Following purification, the CO_2 was expanded into the bellows of a ThermoFinnigan MAT 253 dual inlet mass spectrometer configured to measure M/z 44–49 inclusive for isotopic-ratio analysis (Eiler and Schauble 2004). The Δ_{47} was calculated from the measured 45/44, 46/44, and 47/44 ion ratios of CO_2. All Δ_{47} values were corrected for instrument nonlinearity and scale compression using CO_2 gases heated to 1000°C to achieve the stochastic distribution of isotopologues (Huntington et al. 2009), and mass-48 measurements were used to screen for contaminants. A 90°C acid reaction correction of +0.081‰ was applied to all Δ_{47} data (Passey et al. 2010).

Temperatures of calcite precipitation were calculated from Δ_{47} values using the theoretical calibration of Guo et al. (2009) for calcite because existing calibration data for inorganic calcite (Ghosh et al. 2006; Dennis and Schrag 2010) do not extend to the low Δ_{47} values reported in this study. Precision in temperature estimates, calculated by propagating one-standard-error uncertainties in Δ_{47} through the calcite equation of Guo et al. (2009), range from 2° to 11°C. Temperatures of precipitation, $\delta\ ^{18}O$ values measured simultaneously with clumped isotopes, and the equilibrium fractionation expression of Kim and O'Neil (1997) were used to calculate the $\delta\ ^{18}O_{SMOW}$ of the calcite's parent fluids.

Geomechanical Modeling

Geomechanical modeling was conducted to assess the potential of syndepositional fractures to reactivate, transmit fluids, and drive diagenesis through time. The analysis draws on frictional faulting theory as applied to pre-existing fractures (Jaeger and Cook 1979; Zoback 2007) to calculate the proximity of the syndepositional fractures to frictional failure and episodic slip within the evolving regional stress field (e.g., Morris et al. 1996; Ferrill et al. 1999; Zoback 2007). Previous studies that integrate temperature and production logs with stress analysis and natural fracture interpretations indicate that fractures that are critically stressed for slip in the *in situ* stress state are those that are most permeable (Finkbeiner et al. 1997; Tamagawa and Pollard 2008; Hennings et al. 2012). The same consideration can be applied to the Guadalupian platform carbonates where early fractures were subjected to multiple pulses of advecting fluids.

The reactivation potential of the system of early fractures observed in Dark Canyon was assessed for the major tectonic episodes postdating early fracture formation. We conducted six static stress analyses (Table 1) corresponding to Permo-Triassic burial, early and late Laramide thrusting, early and late Basin and Range extension, and current conditions. Orientation of stress fields and their timing are from Hill (1996). To constrain paleostress gradients, we assumed a constant overburden (S_v) gradient of 0.027 MPa/m and then modified the maximum horizontal stress (S_H) and minimum horizontal stress (S_h) gradients relative to S_v and assumed a S_H orientation based on knowledge of the tectonic setting during the phase under consideration (Table 1). Burial depths for each stress analysis were derived from the burial history of the late Guadalupian section (Hill 1996), and represent the estimated depth of the Tansill Formation at the geologic time modeled. The current-day stress configurations incorporated average *in situ* stress gradients from wellbore stability analyses (e.g., breakouts, induced fractures) within the Delaware Basin (Nolen-Hoeksema et al. 1994).

TABLE 1.—*Input data to the geomechanical analysis.*

	Gradient (MPa/m)	Depth (m)[1]	Stress Direction[1]	Comments
Permo-Triassic burial (~ 230 Mya)				
S_h	0.012	600	70°	normal stress state; horizontal ≈ ½ vertical; S_H slightly
S_H	0.014	600	160°	greater than S_h to represent fracture parallel to margin
S_v	0.027	600	vertical	trend in Dark Canyon
P_p	0.010	600	vertical	
Early Laramide (~ 80 Mya)				
S_h	0.028	600	150°	thrust stress state; S_h and S_v must be similar since thrusting
S_H	0.0405	600	60°	is known to have reactivated normal faults; set $S_H = 1.5S_v$
S_v	0.027	600	vertical	
P_p	0.010	600	vertical	
Late Laramide (~ 40 Mya)				
S_h	0.028	350	150°	weaker thrust setting assumed;set $S_H = 1.25S_v$
S_H	0.03375	350	60°	
S_v	0.027	350	vertical	
P_p	0.010	350	vertical	
Early Basin & Range (~ 20 Mya)				
S_h	0.013	100	80°	normal fault stress state with E-NE tensional stress
S_H	0.02	100	170°	
S_v	0.027	100	vertical	
P_p	0.010	100	vertical	
Late Basin & Range (~ 5 Mya)				
S_h	0.013	100	100°	normal fault stress state with W-NW tensional stress
S_H	0.02	100	10°	
S_v	0.027	100	vertical	
P_p	0.010	100	vertical	
Current conditions (0 Mya)				
S_h	0.0167	100	−30°	average stress gradients
S_H	0.023	100	60°	reported in oil fields in the Delaware Basin (Nolen-
S_v	0.027	100	vertical	Hoeksema et al. 1994)
P_p	0.010	100	vertical	

[1] Depth of assessment and stress directions based on burial and tectonic histories for the Guadalupe Mountain strata, as summarized by Hill (1996).

For each tectonic episode, the applied stress field was resolved onto the plane of a fracture as the effective normal and shear stresses acting along that surface. The amount of additional pore pressure (P_p) necessary to either: (1) bring the effective shear to normal stress ratio to 0.6 and induce shear failure (Byerlee 1978); or (2) exceed the tensile strength of the cement and induce extensional failure was calculated through the application of a hybrid Griffith-Coulomb failure criterion (Sibson 1998) (Fig. 5). The analysis is shown graphically by plotting the stresses on a 3D Mohr diagram along with the Griffith-Coulomb failure criterion. Reactivation potential is reported as the additional pore pressure required to initiate failure (distance from the plotted pole of the fracture plane to the failure envelope; Fig. 5B). A negative value indicates that the fracture is predicted to be reactivated under the applied conditions.

DIAGENESIS OF THE TANSILL OUTER-SHELF FACIES TRACT

To understand the diagenetic fill of the syndepositional deformation features, it is necessary to appreciate the diagenetic history of the adjacent outer-shelf limestones cut by the syndepositional fractures. That diagenetic history is summarized below based on the studies of prior workers, and augmented with observations reported herein. The established paragenetic history of the outer-shelf facies tract (Table 2) contains eight separate events, with events 2 through 5 occurring during early diagenesis. Events 6 and 7, the removal of evaporite minerals and formation of "late" coarse-crystalline calcite spar, are controversial in terms of their timing with respect to the rocks' burial and pore-fluid histories.

Isopachous Cements

Isopachous, circumgranular fibrous and inclusion-rich bladed prismatic cements (Fig. 6A, B) were the first cements formed in outer-shelf deposits. They occur in, and can completely fill, all primary interparticle, intraparticle, and fenestral pores (Schmidt 1977; Rudolph 1978; Parsley and Warren 1989; Mutti and Simo 1994; Mazzullo 1999). The fibrous phase is regarded by all prior workers to originally have been marine aragonite and the prismatic phase to have originally been either high-Mg marine calcite (Given and Lohmann 1986; Garber et al. 1989; Parsley and Warren 1989; Mazzullo 1999) or low-Mg calcite (Mruk 1985, 1989). Microdolomites, 5–10 um in size, occur as inclusions within the isopachous cements and as dolomite crystals atop the fibers. These dolomites also are interpreted to be the byproduct of the isopachous cements' neomorphism (Rudolph 1978; Mazzullo 1999; Rahnis and Kirkland 1999).

Fracturing

The earliest syndepositional fracturing of outer-shelf facies occurred after formation of isopachous cements, as evidenced by the fact that those cement phases are cut by fractures but rarely are observed in fractures (Hunt et al. 2002; Koša et al. 2003; this study). All subsequent diagenetic phases have been observed in, or associated with, fractures (Hunt et al. 2002; Koša et al. 2003; this study), indicating that the onset of fracturing preceded all post-isopachous cementation. Multiple episodes of syndepositional deformation have been identified in outer-platform settings (Hunt et al. 2002; Koša et al. 2003; Koša and Hunt 2005, 2006a; Rush

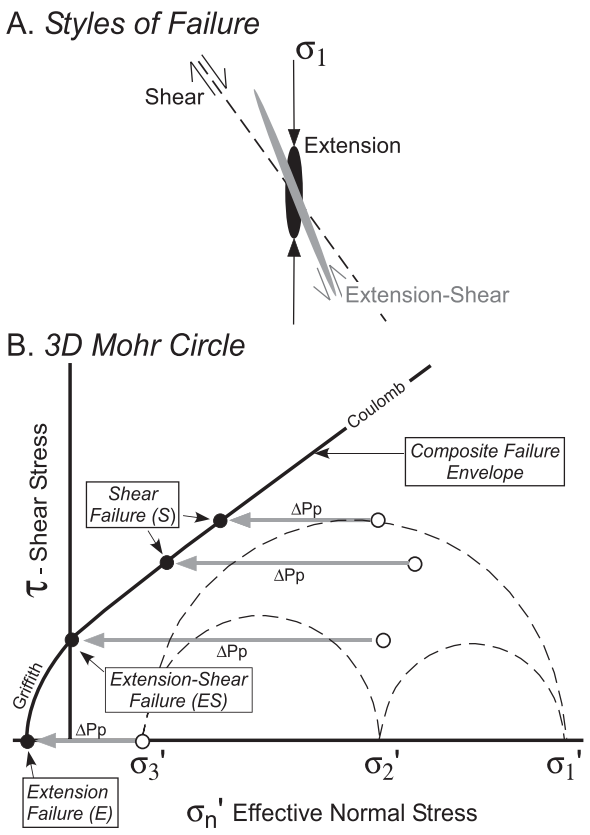

FIG. 5.—**A)** Examples of failure modes predicted for fractures oriented at various angles relative to the maximum principal stress (s_1). An extensional failure mode is most likely for fractures subparallel to s_1 (black); a shear failure mode is most likely for fractures at a moderate acute angle to s_1 (dashed line); and a hybrid extension-shear failure mode is most likely for fractures at intermediate angles to s_1 (gray). **B)** 3D Mohr diagram illustrating assessment of fracture reactivation potential. Solid black line is the Griffith-Coulomb failure criterion, and dashed semicircles denote the differences between the principal stresses. The effective normal and shear stresses resolved on four variously oriented fractures in an applied stress field with effective principal stresses of s_1, s_2, s_3 are represented by the small open dots. The amount of additional pore pressure (ΔPp) necessary to cause failure along those fractures is represented by the gray arrows. The type of failure predicted depends on where those gray arrows intersect the Griffith-Coulomb failure envelope (black dots). Reactivation potential is reported as the pore pressure required to induce failure (ΔPp).

and Kerans 2010; Frost et al. 2012), with complex crosscutting relationships between and within syndepositional fractures.

Dolomitization

Partial and selective dolomitization of originally peloidal and bioclastic micritic grains, particularly originally high-Mg bioclasts, and isopachous cements produced fabric-preserving, very-fine-crystalline dolomite with micro-intercrystalline pores (Fig. 6C, D). Dolomite also occurs as rhombic, fine-crystalline cement (Fig. 6C) that overlies isopachous cements, underlies pore-filling CL-zoned calcite cements, and can be intercalated with calcite cements filling biomolds. Although dolomitization can completely replace host strata proximal to syndepositional fractures (Melim and Scholle 2002; Hunt et al. 2003; Koša and Hunt 2006a; Frost et al. 2012), outer-shelf limestones average ~ 18% dolomite with a range of 0 to 50% (visual estimates, this study). Both replacement dolomite and dolomite cement exhibit a dull reddish luminescence and may have a microns-thick bright red luminescent rim.

Dolomitization of inner- to outer-shelf facies has been interpreted by all prior workers as an early diagenetic feature (Rudolph 1978; Mruk 1985; Parsley and Warren 1989; Garber et al. 1989; Mutti and Simo 1994; Mazzullo 1999; Melim and Scholle 2002). The preference to replace originally high-Mg calcite bioclasts suggests that dolomitization began prior to complete mineralogical stabilization of those grains. Early dolomites are ^{18}O-enriched and are interpreted to have formed from refluxing evaporated seawater (Rudolph 1978; Parsley and Warren 1989; Mutti and Simo 1994; Mazzullo 1999; Frost et al. 2012). Mutti and Simo (1994) showed that dolomitization events were associated with each successive HFS, which explains intercalations of dolomite and calcite in the cements that infill biomolds and some interparticle pores.

Dissolution and Initial Calcite Cementation

Dissolution and precipitation of pore-filling calcite cements are interpreted to have occurred in outer-shelf limestones with the influx of meteoric-derived waters (Rudolph 1978; Garber et al. 1989; Mutti and Simo 1994; Rahnis and Kirkland 1999). The presence of pendant cements and other vadose diagenetic products in shelf-crest facies (Dunham 1972) is unequivocal evidence for subaerial exposure and meteoric influences. Dissolution created moldic pores (now filled with authigenic calcite) in originally aragonitic bioclasts (Rudolph 1978; Garber et al. 1989; Parsley and Warren 1989; Mutti and Simo 1994), enlarged syndepositional fractures (Garber et al. 1989; Mutti and Simo 1994; Hunt et al. 2002; Koša et al. 2003; this study), and corroded isopachous cements (Mazzullo 1999).

The first generation of post-isopachous calcite cement in outer-shelf facies is an equant, inclusion-free, crystalline mosaic with a zoned dull and bright orange CL pattern that crosscuts crystals (Fig. 6A, B). This cement infills molds of originally aragonitic grains, occurs in interparticle pores atop the neomorphosed marine cements, and heals microfractures in outer-shelf limestones (Rudolph 1978; Mutti and Simo 1994; Mazzullo 1999). These earliest calcite cements are depleted in ^{18}O relative to neomorphosed marine isopachous cements (average $\delta^{18}O$ of −8 to −8.5‰ VPDB versus −2.8‰ VPDB, respectively; Mruk 1985, 1989; Given and Lohmann 1986), but are not as depleted in ^{18}O as later calcite spars (Fig. 7A). The early calcite cements in the outer-shelf facies tract are interpreted to be meteoric in origin, probably concurrent with mineralogical stabilization, and having formed during lowstand exposure

TABLE 2.—*General sequence of diagenetic events observed in outer-shelf limestones.*[1]

1. Formation of pore-filling isopachous marine cements.
2. Fracturing.
3. Selective reflux dolomitization of micritic and originally high-Mg calcite bioclasts and precipitation of fine-crystalline rhombic dolomite cements.
4. Meteoric dissolution and precipitation of minor amounts of initial pore-filling calcite cement.
5. Formation of evaporite minerals that replaced, encased, and/or crosscut all grains and prior diagenetic phases, and infilled open pore space.
6. Probable dissolution of some evaporites.
7. Formation of medium to coarse crystalline "late" calcite spars in primary pores, as replacements of evaporites, and in pores created by evaporite dissolution.
8. Teleogenetic (uplift) overprints associated with dissolution and precipitation of speleogenetic calcite.

[1] Based on Schmidt (1977), Rudolph (1978), Parsley and Warren (1989), Garber et al. (1989), Mutti and Simo (1994), Mazzullo (1999), and this study.

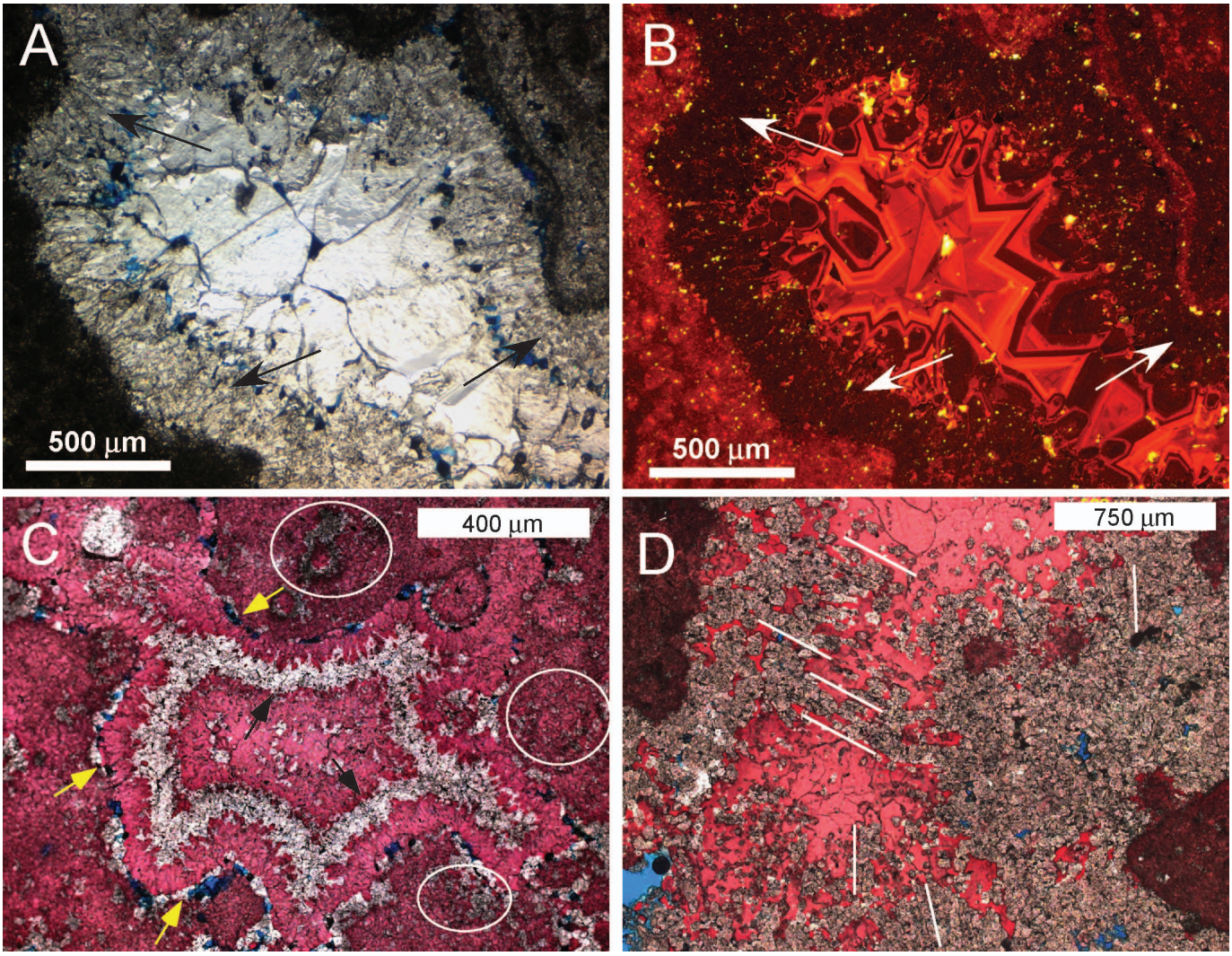

FIG. 6.—**A**, **B)** Paired plane light (left) and cathodoluminescent (right) photomicrographs of fibrous, inclusion-rich isopachous cements that line a primary intergranular pore in outer-shelf limestone (arrows). These cements have a dull red luminescence. They are overlain by zoned, dull red to bright orange luminescent, equant pore-filling calcite cements. The luminescent zonation in those cements crosscuts crystals. **C**, **D)** Dolomite in outer-shelf limestones. Calcite is stained pinkish red; dolomite is unstained (gray, whitish gray). In photomicrograph C, dolomite partially replaces grains (white circles), occurs at the contact between grains and isopachous cements in association with a thin linear mold (yellow arrows), and atop the isopachous cement (black arrows). In photomicrograph D, dolomite partially replaced fibrous marine cements, as evidenced by the elongated "chains" of dolomite crystals (white lines).

between deposition of high-frequency sequences (Rudolph 1978; Given and Lohmann 1986; Mruk 1985, 1989; Parsley and Warren 1989; Mazzullo 1999; this study).

Formation of Evaporite Minerals

Gypsum and/or anhydrite precipitated as idiomorphic and millimeter-scale masses (Fig. 8A, C, E) that crosscut and replaced grains, isopachous cement, dolomite, and early CL-zoned calcite cement (Lucia 1961; Schmidt 1977; Rudolph 1978; Parsley and Warren 1989; Scholle et al. 1992; Mazzullo 1999, this study). Centimeter-scale pseudomorphs of evaporite nodules also are ubiquitous in outer-shelf facies. Scholle et al. (1992) argued that evaporite minerals also precipitated as pore-filling cements and may have been the most common cement type in the outcropping limestones, as they still are today in the subsurface (Garber et al. 1989). Some evaporites probably formed from the same refluxing brines that produced the dolomites, perhaps in an anhydrite precipitation front advancing in front of dolomitization (e.g., Jones and Xiao 2005). Other evaporites may have formed from brines refluxing downward during deposition of overlying Permian evaporite-rich units.

In spite of their apparent initial abundance in outer-shelf facies, no evaporites remain in outcrop; they have been either subsequently calcitized or dissolved. The calcitized evaporites are now recognized by their nodular shape, inclusions of "floating" dolomite rhombs within the calcites that replaced the anhydrites (Lucia 1961; Rudolph 1978; this study), crystal pseudomorphs of anhydrite (Rudolph 1978; Parsley and Warren 1999; Mazzullo 1999; this study), rare inclusions of remnant anhydrite (Scholle et al. 1992; Mazzullo 1999), or other criteria related to the nature of the calcite spars that replaced the evaporites (detailed below).

Calcite Spars

In addition to the earliest formed meteoric calcite cements described above, medium- to coarse-crystalline, ^{18}O-depleted authigenic calcites occur in outer-shelf through fore-reef facies tracts. These late calcite spars

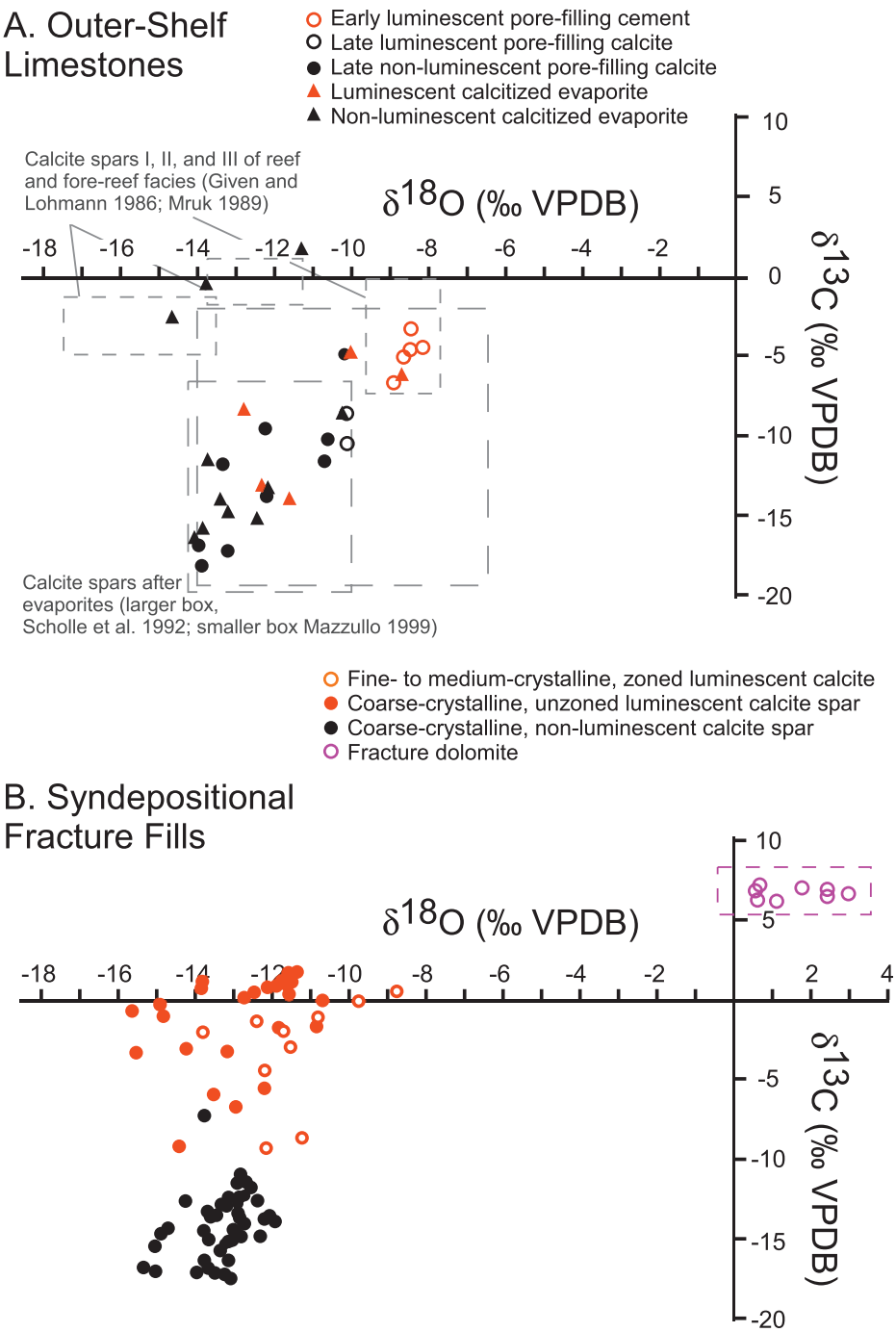

FIG. 7.—Cross plots of stable-isotope data for **A)** authigenic calcites in outer-shelf limestones and **B)** calcite and dolomite in syndepositional fractures. Fracture data includes analyses of microsamples and clumped-isotope samples.

exhibit three luminescent patterns. The most common is non-luminescent calcite spar (Schmidt 1977; Rudolph 1978; Mutti and Simo 1994; Mazzullo 1999; this study) that may be pitted with microvoids, occurs in evaporite pseudomorphs (Fig. 8C, D), moldic and interparticle pores (Fig. 9A, B), and rarely contains two-phase aqueous or hydrocarbon inclusions (this study). The late non-luminescent calcite spars in Dark Canyon have $\delta^{18}O$ values ranging from −10.1 to −16.2‰ VPDB and $\delta^{13}C$ values ranging from +1.9 to −18.1‰ VPDB (Fig. 7A). Less common is a luminescently zoned (initially dull red or non-luminescent core, then bands of bright and dull orange) medium to coarse-crystalline calcite spar (Schmidt 1977; Mazzullo 1999; this study), which occurs in evaporite pseudomorphs (Fig. 8A, B) and interparticle pores (Fig. 9C, D). The zonation can indicate growth from the pore walls to the pore center or growth from the pore center to the pore walls. The final bright CL zone thus may onlap the luminescent prismatic calcites sitting atop the isopachous cements (Fig. 9D), have a pore between themselves and the isopachous cements, or grow over to and now sit atop any hydrocarbon staining on younger cements (Scholle et al. 1992). Prior workers report the luminescent calcite spar to be younger than (i.e., overlie) the non-luminescent calcite spar (Schmidt 1977; Mazzullo 1999), a relationship confirmed in this study in the rare cases in which both phases were observed in the same pore (Fig. 8F). The third and rarest CL pattern in calcite spars is a rectilinear or felted pattern inherited from an evaporite precursor (Fig. 8F). Isotopically, the luminescent calcite spars have $\delta^{18}O$ values

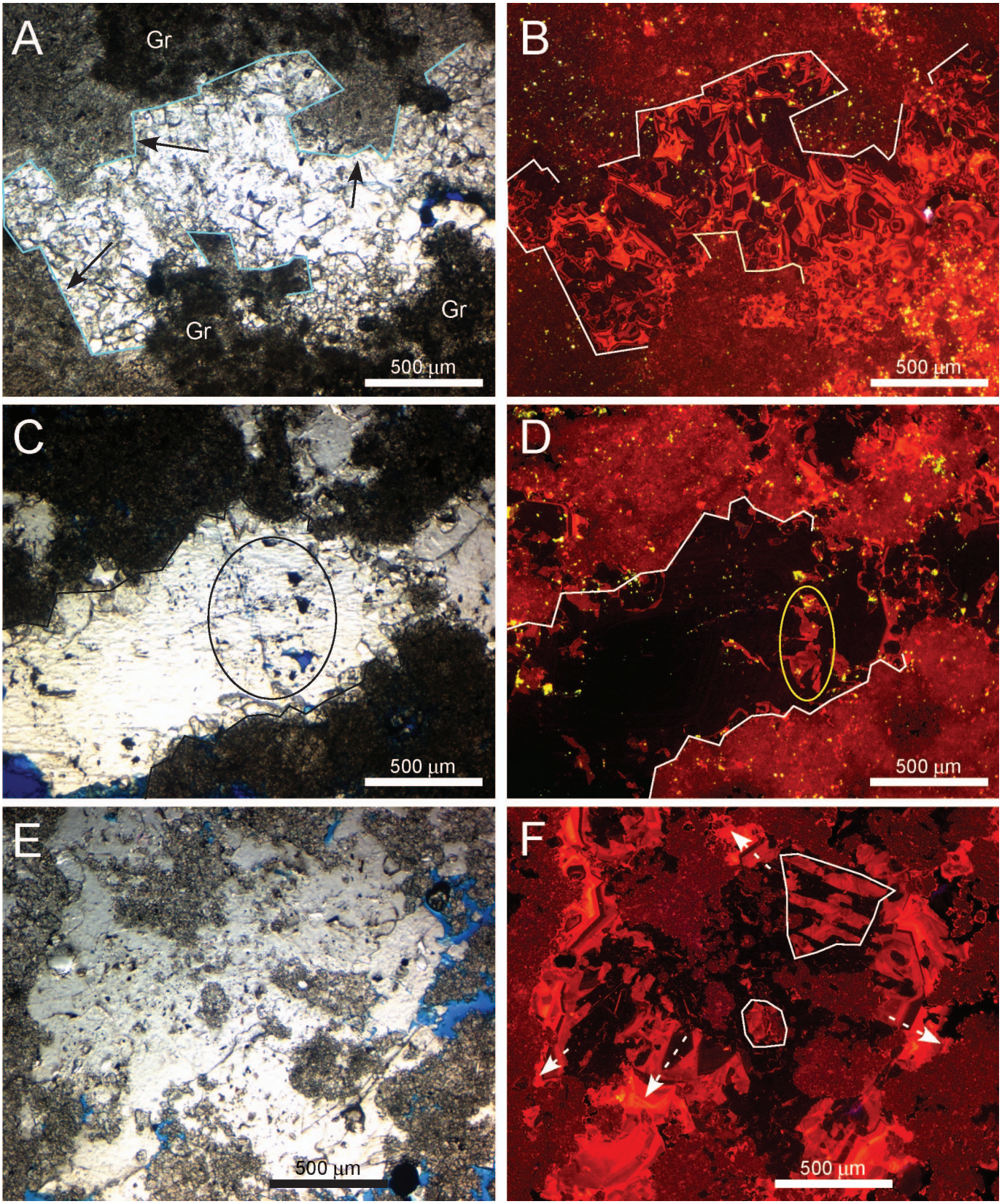

FIG. 8.—Paired plane light (left) and cathodoluminescent (right) photomicrographs of evaporite pseudomorphs and late calcite spars. **A**, **B)** Evaporite pseudomorph crosscuts grains and isopachous marine cements (arrows). Blue lines outline the rectilinear boundaries of the former evaporite. The luminescence pattern of the calcite (non-luminescent cores with bands of bright orange overgrowth) indicates that calcite crystals grew from multiple nucleation sites on the walls of the pseudomorph and

ranging from −8.8 to −12.9‰ VPDB and $\delta^{13}C$ values ranging from −4.6 to −13.8‰ VPDB (Fig. 7A).

Many luminescent and non-luminescent calcite spars, including those that fill primary pores, have an origin related to the alteration of evaporites. Evidence includes: their association with evaporite pseudomorphs; evaporite crystal morphologies in CL patterns; ghosts of grains floating in the calcite spar (Scholle et al 1992); truncated patches or earlier-formed luminescent calcites embedded in the calcite spars (Fig. 8D, F); millimeter-scale masses that crosscut depositional fabrics; and the calcite crystals growing from pore centers to pore margins, which is not a normal pore-filling cementation pattern. However, in some interparticle and moldic pores there is no evidence that these calcite spars are related to evaporite alteration. Nonetheless, Scholle et al. (1992) argued that the latter also represented calcite after evaporites, but other workers were mute on that possibility (Mutti and Simo 1994; Mazzullo 1999) or argued against it (Hill 1996).

The isotopic data collected herein for the late calcite spars suggest that they were derived from a variety of fluid systems. For example, one luminescently zoned coarse calcite spar in a calcitized evaporite pseudomorph has the same isotopic composition as the syndepositional meteoric calcite cements (Fig. 7A), suggesting that a first stage of evaporite calcitization occurred in association with subaerial exposure atop HFS packages. Mutti and Simo (1994) and Mazzullo (1999) also thought that some calcite spars were related to HFS subaerial exposure. A second group of late calcite spar is represented by three non-luminescent calcite spars in calcitized evaporites (Fig. 7A) that have the same oxygen (−10.8 to −15.5‰ VPDB) and carbon (–2 to +2‰ VPDB) isotopic compositions as allegedly Permian groundwater spars (Mruk 1985, 1989; Given and Lohmann 1986). A third, and dominant group of late calcite spars are represented by the luminescent and non-luminescent phases that have a wide range of negative $\delta^{18}O$ and $\delta^{13}C$ values. The highly varied luminescence and isotopic characteristics imply multiple calcitization events in waters of varied eH, temperature, and oxygen isotope composition. The extremely negative $\delta^{13}C$ values imply microbial degradation of hydrocarbons (Wiggins et al. 1983), which Scholle et al. (1992), Wiggins et al. (1993), Mazzullo (1999), and Melim and Scholle (1999) interpreted to implicate Tertiary flushing with meteoric fluids. However, warm fluids derived from basinal sources cannot be excluded (Schmidt 1977; Mruk 1989; Hill 1996), particularly since Crysdale (1987) reported fluid-inclusion temperatures of 50° to nearly 100°C for late calcite spars in the reef and fore-reef facies tracts.

Teleogenetic Overprints

Two diagenetic features formed in the outer-shelf limestones in association with teleogenetic uplift (Schmidt 1977; Rudolph 1978; Mutti and Simo 1994; Hill 1996). These features are vuggy pores produced by the partial dissolution of coarse-crystalline calcites and laminated, brown, micrite to fine-crystalline, pendant calcite (Fig. 9E, F). The calcite is non-luminescent, but weakly fluoresces white. Crosscutting relations make these phase the last events in the limestones paragenesis, which led all prior workers to assign their origin to late Tertiary or Quaternary near-surface and/or outcrop events.

RESULTS—FRACTURE FILLS

Petrographic Observations

Each syndepositional fracture exhibits a unique paragenetic history or a history that is similar to one or more of the other sampled fractures. In common to the widest fractures is a dominance of coarse-crystalline, inclusion-rich calcite spar (Fig. 4B, D). Five different paragenetic fills, each from a separate fracture, provide insight into the most common diagenetic sequences.

Fill A.—This fracture fill (Fig. 10) shows ostracod wackestone sediment that infiltrated into the fracture (host rock is skeletal–peloidal packstone). Gypsum precipitated in the crack and partially replaced the ostracod sediment, as evidenced by gypsum pseudomorphs. Gypsum then dissolved and the pseudomorphs were filled with a fine-crystalline mosaic of zoned, orange-luminescent calcite. That mosaic exhibits increasing crystal size and concentric CL zonation into the pore, features that indicate growth as a pore-filling cement. Precipitation of medium-crystalline, non-luminescent to zoned orange-luminescent calcite cement followed. The outer luminescent portion of that cement phase was then corroded. Another generation of calcite then precipitated, this one containing inclusion-rich bands and exhibiting no luminescence. Its outer margin was also corroded by dissolution. That corrosion surface is overlain by weakly fluorescent laminated micritic and very fine-crystalline calcite that lines the pore in the center of the fracture fill.

Fill B.—The walls of this fracture are dolomitized, and that dolomite extends as a halo for a few centimeters into the host limestone on both sides of the fracture. A rim of isopachous, fine-crystalline dolomite cement (dull-red luminescence) lines the fracture wall (Fig. 11). Overlying the dolomite is medium- to very coarse-crystalline calcite that has a non-luminescent core and CL-zoned orange luminescent overgrowths. The core and initial luminescent overgrowths were corroded and fractured, and then healed by additional bright orange luminescent calcite overgrowths. These relations indicate that the luminescently zoned calcite was forming concurrent with episodic fracturing and dissolution.

Fill C.—This fracture (Fig. 12) contains a chaotic, polymictic breccia that extends for ~ 1.5 cm into the fracture and is cemented by medium-crystalline, CL-zoned, orange luminescent calcite cement. One breccia clast has been replaced by micro-void-bearing, non-luminescent calcite that contains micritic inclusions that indicate the original presence of the clast (Fig. 12B). This non-luminescent calcite is interpreted to be a replacement of an evaporite mineral that had originally replaced the clast or the host limestone from which the clast was derived. The breccia and

←

within the pseudomorph. This observation in turn suggests that the evaporite may have first dissolved and the calcite is a pore-filling cement. **C**, **D)** Coarse-crystalline calcite spar with numerous inclusions and blue-epoxy filled microvoids (black circle) in an evaporite pseudomorph. All of the calcite is non-luminescent, but it includes irregularly shaped patches of orange luminescent bands (yellow oval). The bands are truncated and irregularly shaped; they are inclusions of an earlier generation of calcite cement that was an inclusion in the evaporite pseudomorph and are now inclusions in the calcite spar. This suggests that the non-luminescent calcite spar replaced evaporite minerals, otherwise the relict cement inclusions would have collapsed to the floor of the pseudomorph when the evaporite dissolved. **E**, **F)** Millimeter-scale, calcite-filled evaporite pseudomorph contains inclusions of dolomitized grains and isolated dolomite crystals "float" in the calcite mass. The calcite spar after the evaporite exhibits complex luminescence patterns. Black, non-luminescent calcite includes truncated relicts of an earlier formed calcite cement with zoned orange luminescence (outlined in white). The non-luminescent calcite surrounding the larger mass of relict calcite exhibits rectangular (lath-like) shapes. These observations indicate the non-luminescent calcite replaced evaporite minerals. Elsewhere, a later generation of luminescently zoned calcite spar (very dull to bright orange bands) grew from the non-luminescent calcite towards the margins of the pseudomorph (dashed white arrows). This calcite spar is interpreted to be cement that formed after the evaporite not replaced by calcite dissolved.

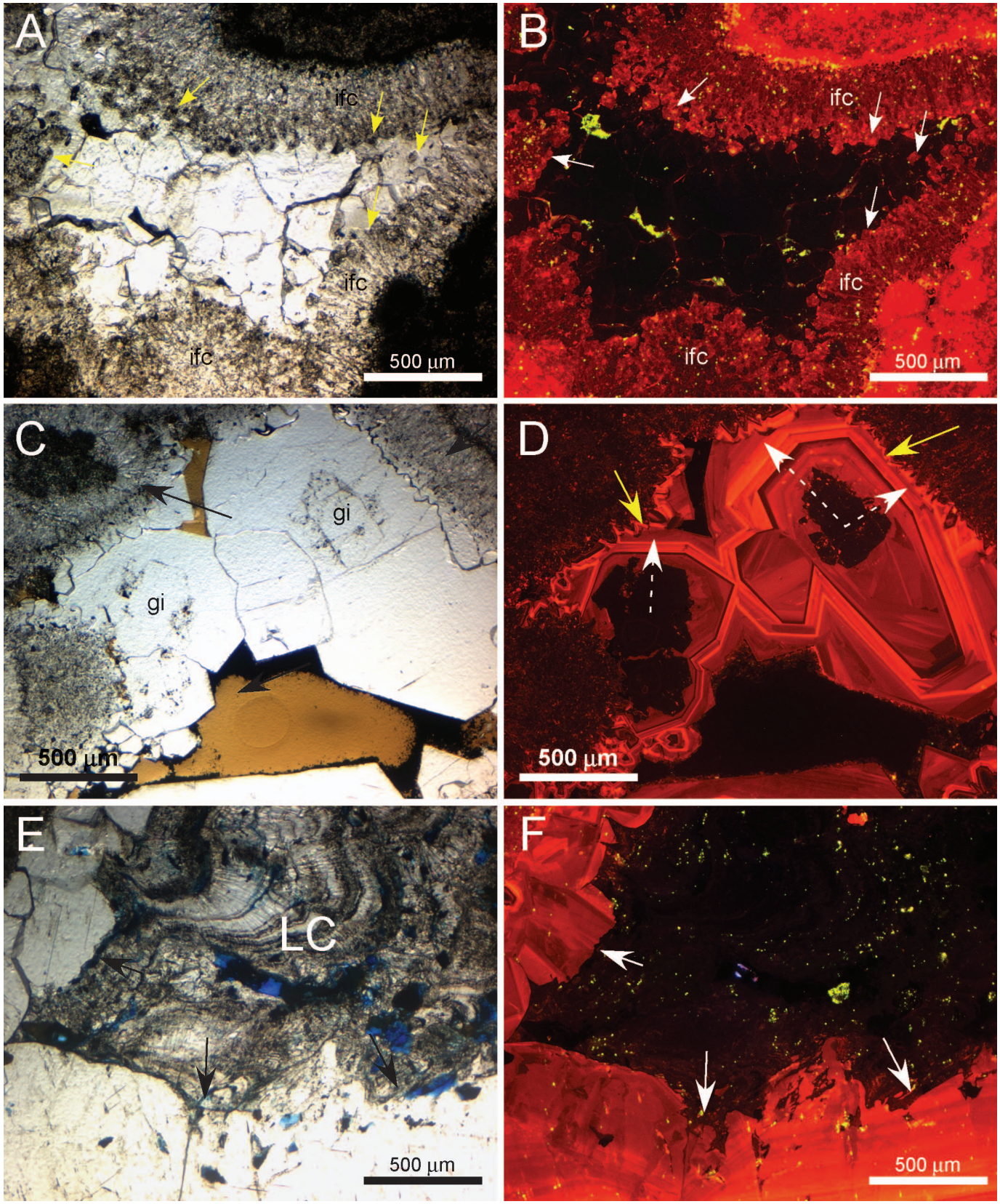

FIG. 9.—Paired plane light (left) and cathodoluminescent (right) photomicrographs of late calcite spars. **A**, **B)** Non-luminescent coarse-crystalline calcite spars fill the center of an intergranular pore. Isopachous fibrous cements (ifc) line the pore walls and exhibit dull red luminescence. Fine crystalline, dull red luminescent dolomite rhombs occur between the two calcite phases (arrows). **C**, **D)** Isopachous cements (black arrows) line grains; the remaining interparticle pore is occupied by luminescently

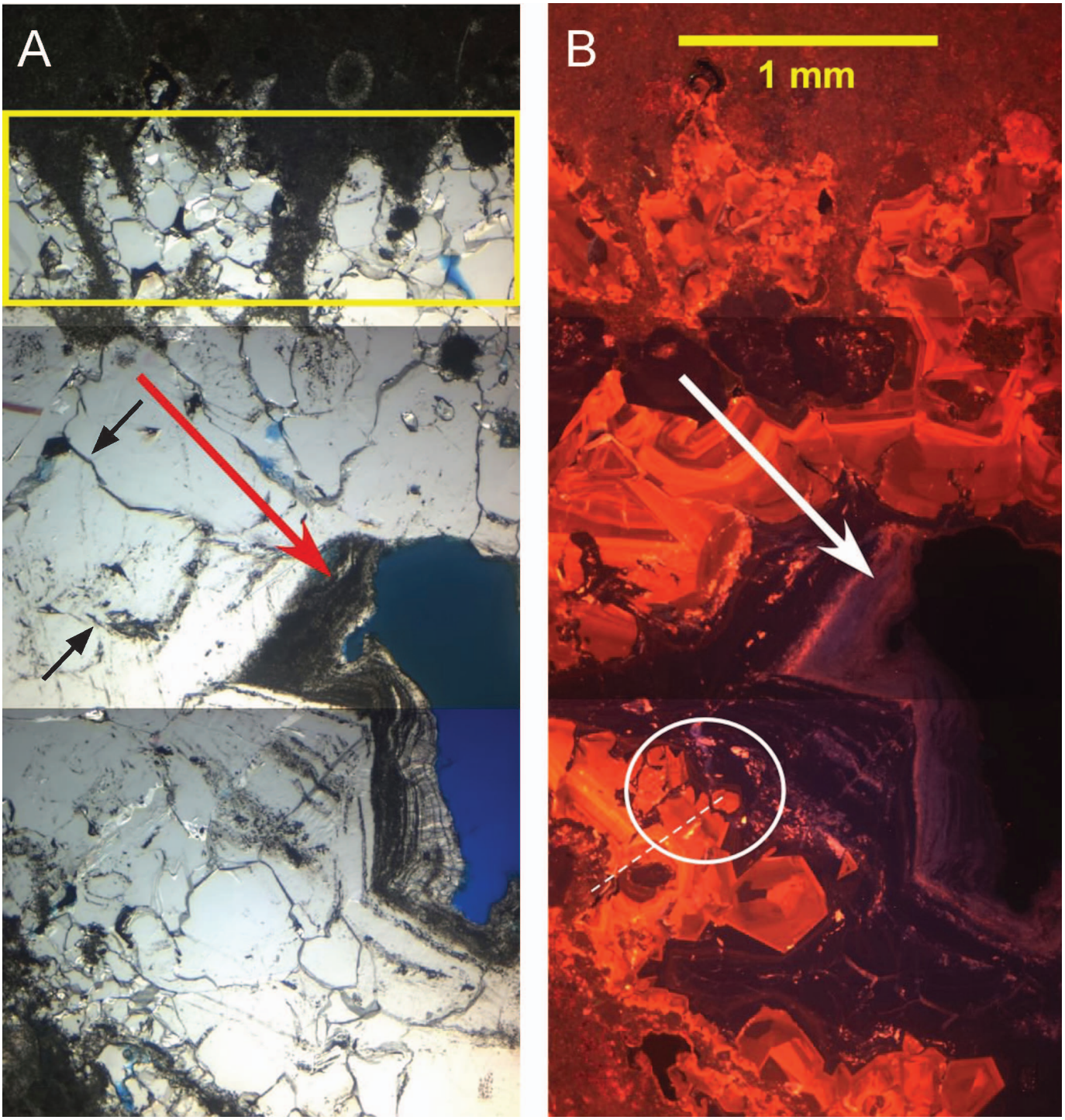

FIG. 10.—**A)** Paired plane light and **B)** cathodoluminescent photomosaics through fracture fill A. Ostracod wackestone at the top of the image infiltrated into the syndepositional fracture and lines one fracture wall. Crystal pseudomorphs of gypsum (yellow box) partially replace the wackestone. The gypsum was replaced with a fine-crystalline, orange luminescent calcite. The main fracture fill (red and white arrows) begins with a luminescently zoned (dull to bright orange) calcite (dashed white line). This cement includes inclusions (black arrows) that outline a rectangular precursor, interpreted to be either a former evaporite crystal or evaporite replaced sediment. The outermost CL zones are broken and corroded (circle). Non-luminescent calcite heals those dissolution features, cements the broken luminescent cement, and fills the balance of the fracture. It is overlain by a laminated, non-luminescent calcite (tip of the arrows).

←

zoned calcite cement initiated on some type of ghost inclusion (gi). The CL-zoned cement grew from that inclusion (former evaporite crystal?) towards the margins of the pore (white arrows). **E**, **F)** Vuggy pore contains fine to coarse-crystalline, orange luminescent calcite spar that is corroded along its edges (arrows) and then overlain by interlaminated fine-crystalline calcite and micrite (LC) that is non-luminescent. The laminated precipitates are interpreted to be teleogenetic.

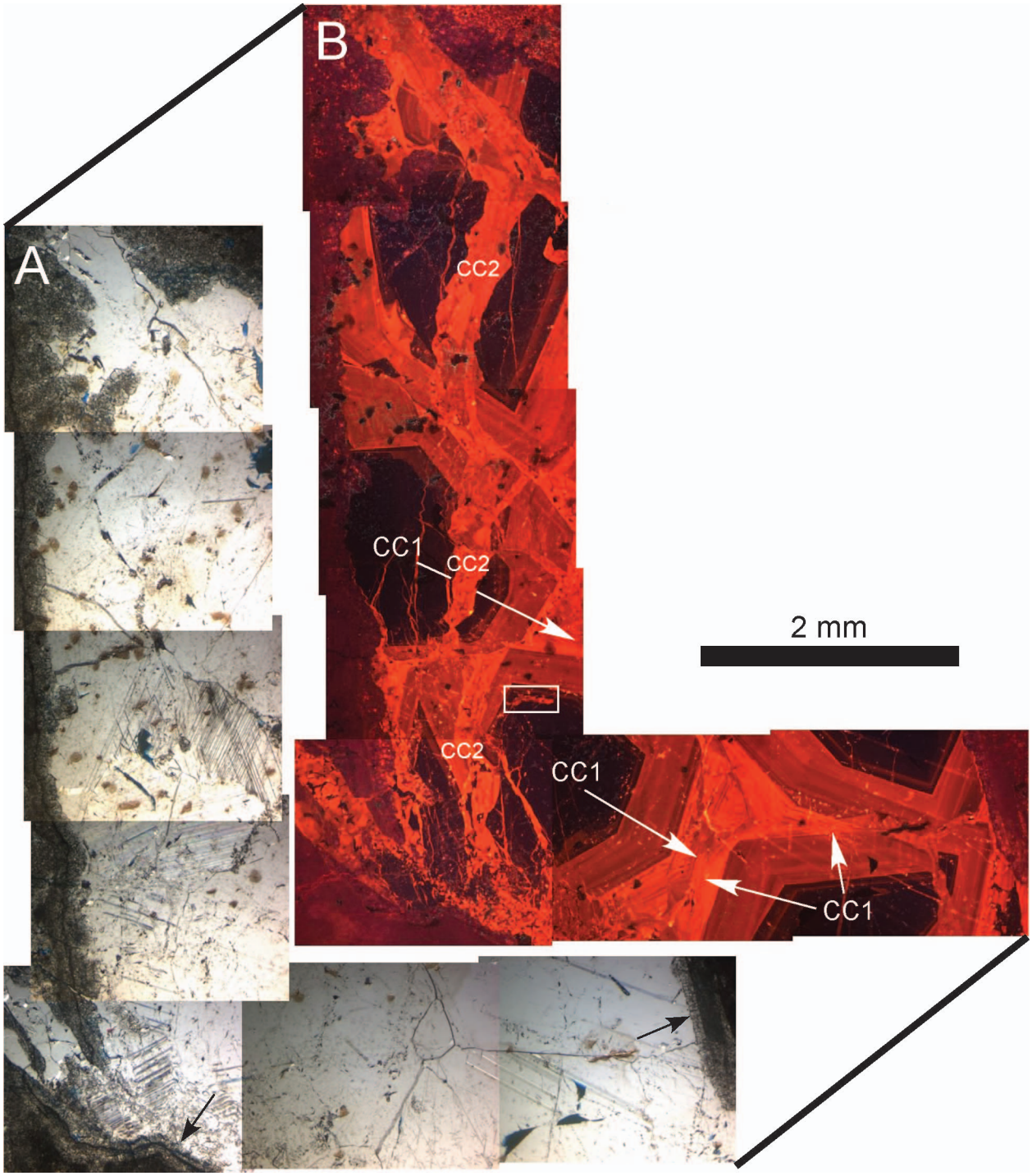

FIG. 11.—**A)** Paired plane light and **B)** cathodoluminescent photomosaics through fracture fill B. The wall of the large fracture is lined with bladed dolomite cement (black arrows). Overlying the dolomite is a first generation of luminescently zoned (non to dull to bright orange) calcite cement (CC1). With subsequent refracturing,

→

FIG. 12.—Paired plane light (left) and cathodoluminescent (right) photomicrographs from fracture fill C. **A**, **B)** Margin of the fracture contains chaotic breccia clasts cemented by a luminescently zoned calcite cement. The ghost of a replaced clast (g) is marked by inclusions in the calcite spar; it is interpreted to represent calcitized anhydrite. **C**, **D)** Luminescent cements within the breccia fill are slightly etched and perhaps rotated (arrows, white box). **E**, **F)** Coarse-crystalline, orange luminescent calcite occupies most of the 7-cm-wide fracture. It is highly pitted (microvoids) and contains former microvoids that are infilled (“healed”) with bright yellow and yellow-orange luminescent calcite (arrows). One millimeter scale bar in photomicrograph F is applicable to all images.

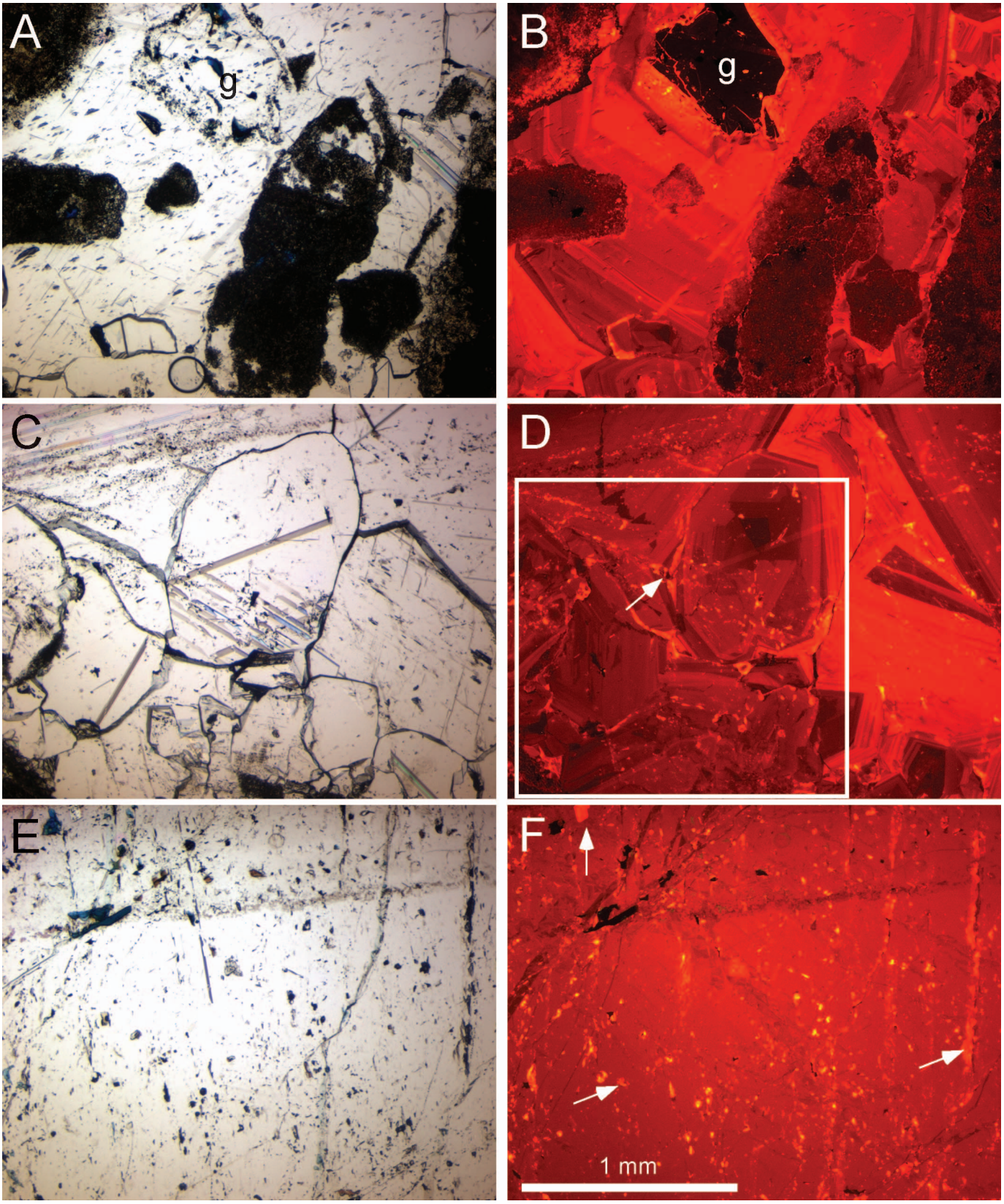
A
g
B
g
C
D
E
F
1 mm

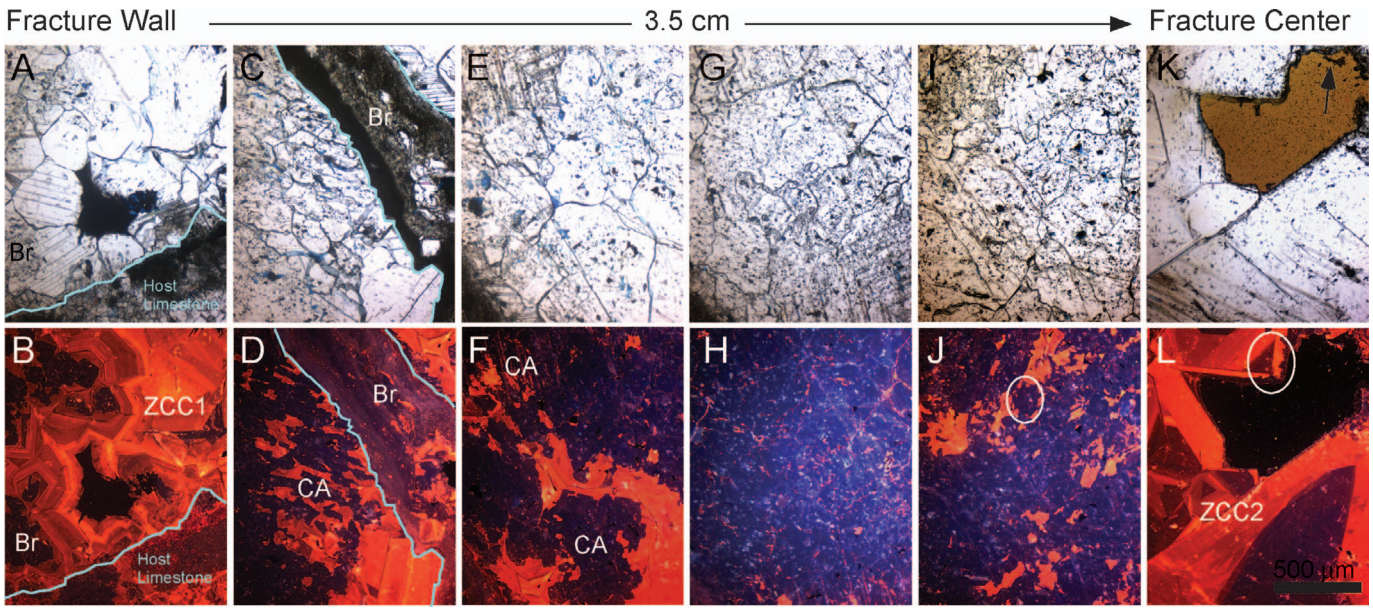

FIG. 13.—Mosaic of paired plane light (upper) and cathodoluminescent (lower) photomicrographs across fracture fill D. Fracture wall is to the left, fracture center is to the right. Scale bar in the lower right is applicable to all images. **A**, **B)** An initial luminescently zoned calcite cement (ZCC1) occurs at the fracture wall (far right) and partially encases breccia clasts (Br). **C**, **D**, **E**, **F)** Coarse-crystalline, inclusion-rich non-luminescent calcite that exhibits irregular patches of orange luminescent calcite. The two luminescent phases crosscut individual calcite crystals, and the elongate and rectangular CL patterns are suggestive of an anhydrite precursor. That is, the non-luminescent phase is calcitized anhydrite (CA) and the luminescent phase is calcite cement filling voids where anhydrite dissolution occurred during replacement. **G**, **H)** Non-luminescent calcite dominates farther into the fracture fill. **I**, **J)** Close to the fracture center the non-luminescent phase can include hydrocarbon inclusions (within white circle) and the non-luminescent phase contains many dissolution pits that have been backfilled with orange luminescent calcite cement. **K**, **L)** At the fracture center, another zoned orange luminescent calcite cement (ZCC2) overlies the non-luminescent calcite that dominates the fracture fill. This luminescent phase contains dissolution pits on its crystal surfaces (white circle) that are in turn overlain by non-luminescent microcrystalline calcite (black arrow in plane light image) interpreted to be teleogenetic.

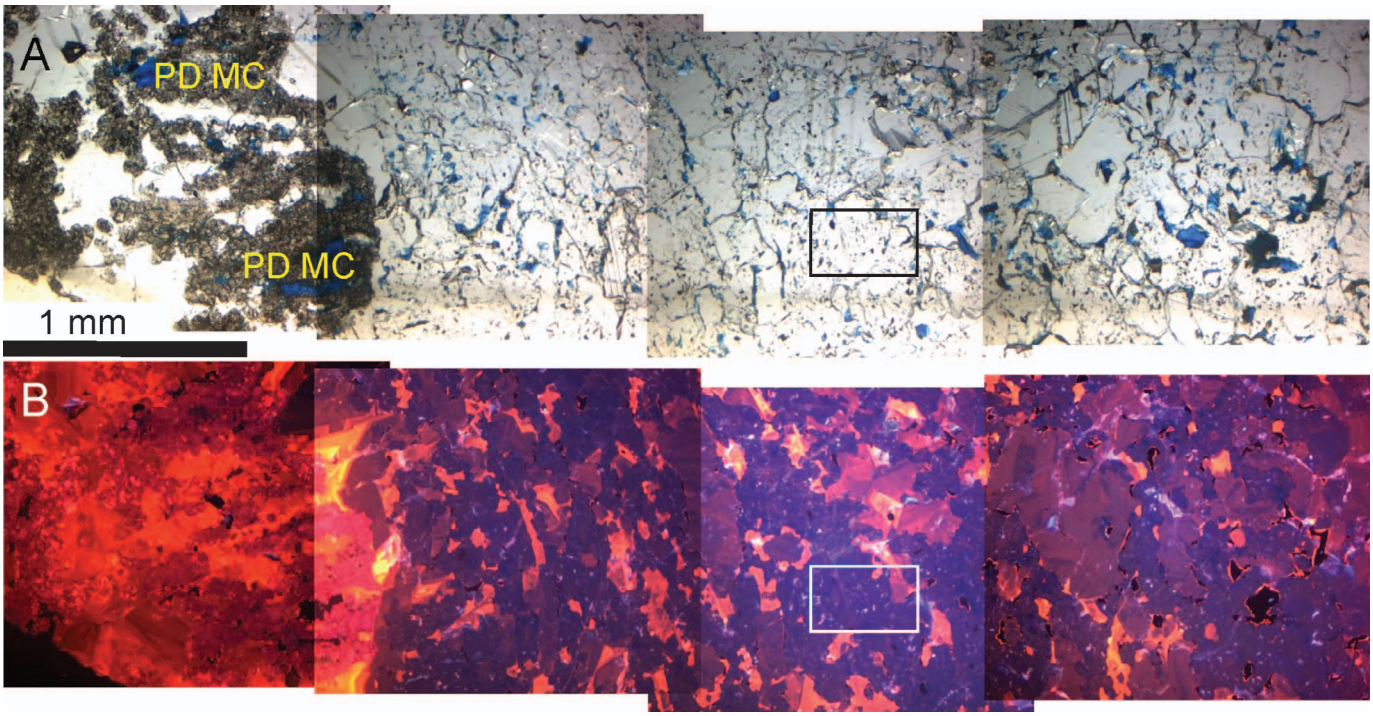

FIG. 14.—**A)** Paired plane light and **B)** cathodoluminescent photomosaics through fracture fill E (same fracture as in Fig. 4C). Isopachous marine cements were partially dolomitized (PD MC) and partially dissolved. The calcite cement filling the dissolution voids in the former isopachous cement is bright orange luminescent. Most of the crack to the right of the dolomite is filled with inclusion-rich and pitted non-luminescent calcite spar that has microvoids back-filled with an orange luminescent "healing" calcite. Hydrocarbon fluid inclusions (Fig. 15) occur in the non-luminescent calcite within the outlined boxes.

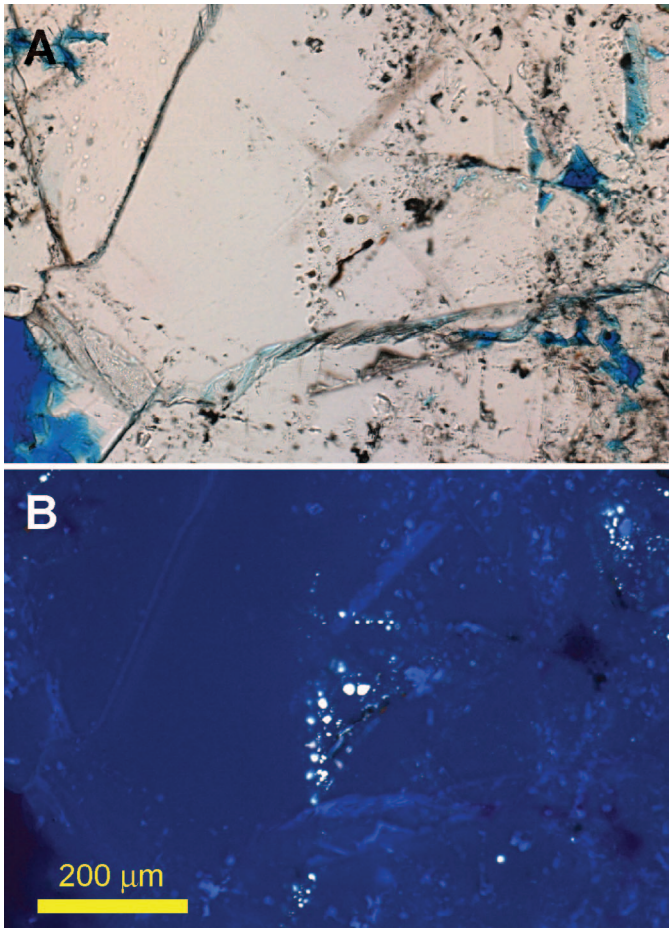

FIG. 15.—Paired **A)** plane light and **B)** fluorescent photomicrographs of fracture-filling calcite spar with white fluorescence that indicates hydrocarbon-bearing fluid inclusions.

its encasing CL-zoned cement is in turn overlain by a unzoned, orange luminescent, very coarse-crystalline, inclusion-rich calcite that extends for 2.5 centimeters to the center of the fracture (Fig. 12E, F). This calcite contains numerous open microvoids and some bright orange luminescent calcite that heals other microvoids.

Fill D.—The next fill (Fig. 13A, B) shows medium crystalline, zoned, orange luminescent calcite along the fracture wall. The zonation crosscuts crystals and indicates cement growing into an open pore. About 0.5 cm into the fracture, that calcite cement is overlain by inclusion- and microvoid-rich coarse-crystalline calcite that exhibits felted, rectilinear, and irregular patterns of dull, non, and bright luminescence (Fig. 13C–F). The rectilinear and lath-like CL structures indicate that this CL pattern was inherited from an anhydrite precursor that the calcite replaced. In fill D, the now-vanished anhydrite presumably was cement formed atop the CL-zoned calcite that formed on the fracture wall. The calcite with the irregular CL pattern is overlain by inclusion-rich, coarse- to very-coarse crystalline non-luminescent calcite (Fig. 13G–J) that contains many open microvoids and orange-luminescent patches that heal other microvoids. The non-luminescent phase extends for 6 centimeters to the center of the fracture. At the very center of the fracture, the non-luminescent calcite is overgrown by calcite cement that exhibits CL-zoned orange luminescence (Fig. 12K, L). That overgrowth in turn is corroded lightly and overlain with trace amounts of weakly fluorescent laminated micritic calcite.

Fill E.—The remnants of a partially dolomitized cement line the wall of the fifth example of fracture fill (Fig. 14). The dolomite crystals exhibit dull red luminescence and are aligned in elongate patterns that suggest that the original phase was fibrous aragonite. The precursor that was not dolomitized was dissolved, and the void space was filled with bright orange luminescent calcite. The balance of the fracture is filled with coarse- to very coarse-crystalline, non-luminescent calcite cement that contains numerous microvoids and fluid inclusions, some of which contain fluorescent hydrocarbons (Fig. 15). Irregular patches of orange luminescent calcite occur throughout the non-luminescent calcite (Fig. 14). Some of these patches heal small irregular voids in the non-luminescent calcite. Others are larger and of an uncertain origin, but their irregular CL character suggest that they are not pore-filling cements. Swarms of micro cracks filled with luminescent calcite also cut the non-luminescent phase (Fig. 16), indicating reactivation of the fractures after formation of the coarse calcite spars.

Geochemical Results

Stable-Isotope Data.—The stable-isotope composition of dolomitized fracture walls and dolomitized cements (Fig. 7B) overlap with the isotopic compositions of early replacive dolomites in the host strata reported by Frost et al. (2012). Fine- to medium-crystalline, luminescently zoned early calcite cements have $\delta^{18}O$ values of −8.8 to −14.0‰ VPDB and $\delta^{13}C$ values of +0.7 to −9.1‰ VPDB. That range in $\delta^{13}C$ is similar to the range exhibited by early pore-filling cements in the host limestones, but the $\delta^{18}O$ values are, on average, ~ 2‰ more negative than early calcite cements in host limestones (Fig. 7A vs. B). Non-luminescent coarse-crystalline fracture spars exhibit a relatively narrow range in $\delta^{18}O$ values (−12 to −15.8‰ VPDB) and $\delta^{13}C$ values ranging from −11.0 to −17.1‰ VPDB. Plotted as a function of distance from the fracture wall (Fig. 17), non-luminescent spars have invariant isotope compositions across any single fracture fill. With a few exceptions, the stable-isotopic compositions of the non-luminescent fracture fills are similar to the isotopic compositions of non-luminescent pore-filling cements and non-luminescent calcified evaporite masses in outer-shelf limestones (Fig. 7). In contrast, the unzoned, coarse-crystalline orange luminescent spars in the fractures have a broad range in $\delta^{18}O$ values (−10.7 to −15.5‰ VPDB), and $\delta^{13}C$ values ranging from +2 to −9‰ VPDB. The luminescent spars also show variations in both $\delta^{13}C$ and $\delta^{18}O$ with distance from fracture walls (Fig. 17) and many are more depleted in ^{18}O but more enriched in ^{13}C than the late luminescent pore-filling cements and luminescent calcified evaporite masses in host limestones (Fig. 7).

Fluid-Inclusion Data.—All fluid inclusions analyzed were in late calcite spars, the inclusions were two phase, and many were hydrocarbon bearing. Homogenization temperatures range from 50°C to 155°C for all 136 analyses. Forty-seven inclusions were large (> 80 µm^2) and/or elongate with a length-to-width ratio > 3, characteristics that could mean stretching and resetting of inclusions since their formation (Goldstein and Reynolds 1994). Disregarding the large and/or elongate inclusions, late calcite spars with orange luminescence have homogenization temperatures (Fig. 18A) ranging from 51° to 75°C (median = 57°C), and the non-luminescent calcite spars exhibit homogenization temperatures ranging from 57° to 105°C (median = 74°C).

Freezing temperatures, which reflect the salinity of the fluid in the inclusions, were acquired on 64 inclusions, of which 40 were small and not elongated. Freezing temperatures for those 40 inclusions range from 0.1 to −14.0°C (Fig. 18B). Using the Bodnar NaCl model (cf. Goldstein and Reynolds 1994), those data indicate a broad range of salinities ranging from freshwater to a brine of 17.8 wt % NaCl. Some individual fractures exhibit a narrow cluster of freezing and homogenization temperatures, whereas others exhibit a broad range (Fig. 18B).

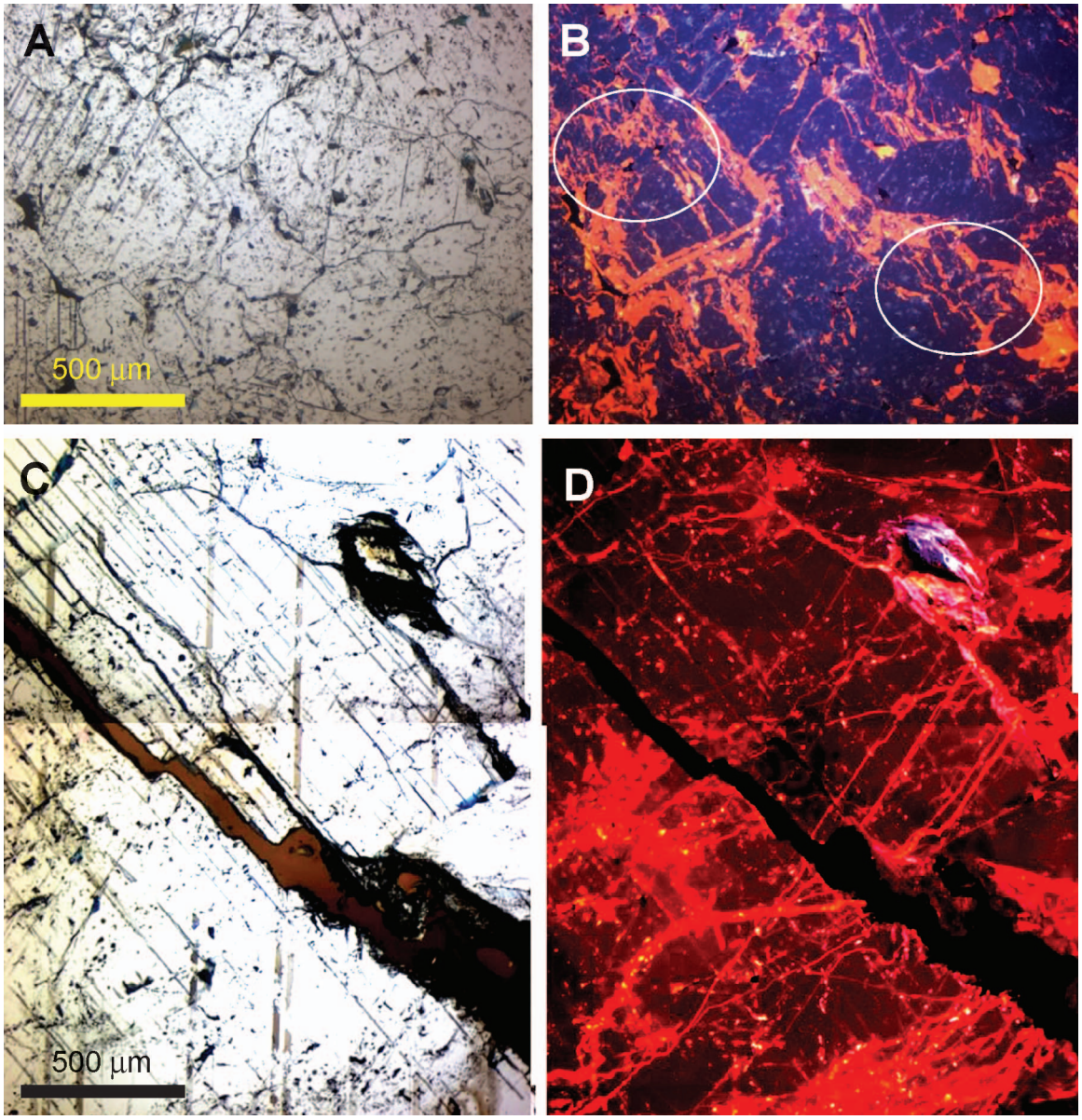

FIG. 16.—**A**, **B)** Paired plane light (left) and cathodoluminescent (right) photomicrographs illustrating evidence for microfracturing, dissolution, and rotation (white ovals) of non-luminescent calcite spars. The irregular microvoids created are infilled with orange luminescent calcite. **C**, **D)** Paired plane light (left) and cathodoluminescent (right) photomicrographs showing orange luminescent calcite healing swarms of microfractures through the non- to very dull red- luminescent fracture filling.

The only previous study of two-phase fluid inclusions in any of the Permian carbonates of the Guadalupe Mountains was the work of Crysdale (1987), who examined calcite spars in the reef and fore-reef deposits of the massive Capitan reef facies. She reported homogenization temperatures of 48°C to 100°C for primary inclusions, with a lower average (64°C) in an earlier generation of calcite spar and a slightly higher average (80°C) in a later generation of calcite spar. Both phases had freezing temperatures ranging from −2.5 to 0°C, indicative of low-salinity fluids. Crysdale (1987) also noted secondary fluid inclusions with a similar range in homogenization temperatures but with freezing temperatures indicative of highly saline fluids (13–20 wt % NaCl). The fluid-inclusion data reported herein overlap with the entire suite of values obtained by Crysdale (1987).

Clumped-Isotope Thermometry.—The clumped-isotope paleothermometer data (Table 3) reveal three distinct groups of calcites, defined by their temperatures and waters of formation, luminescence character, and $\delta^{13}C$ values. The first group comprises the initial CL-zoned cements along fracture walls and around breccia clasts, which have $\delta^{13}C$ values greater than −9‰ and formed at 16°C (reef facies) and 22° to 32°C (outer-shelf facies) in waters with $\delta^{18}O_{smow}$ values that ranged from −6.2 to −10.5‰. The second group contains the coarse-crystalline, orange luminescent calcite spars with abundant fluid inclusions and microvoids that also have $\delta^{13}C$ values greater than −9‰ but formed at 59° to 65°C (reef facies) and 81°C (outer-shelf facies) in waters of with $\delta^{18}O_{smow}$ values of −2.1 to −4.0‰ (average −3.1‰). The third group comprises coarse-crystalline, non-luminescent calcite spars with $\delta^{13}C$ values less

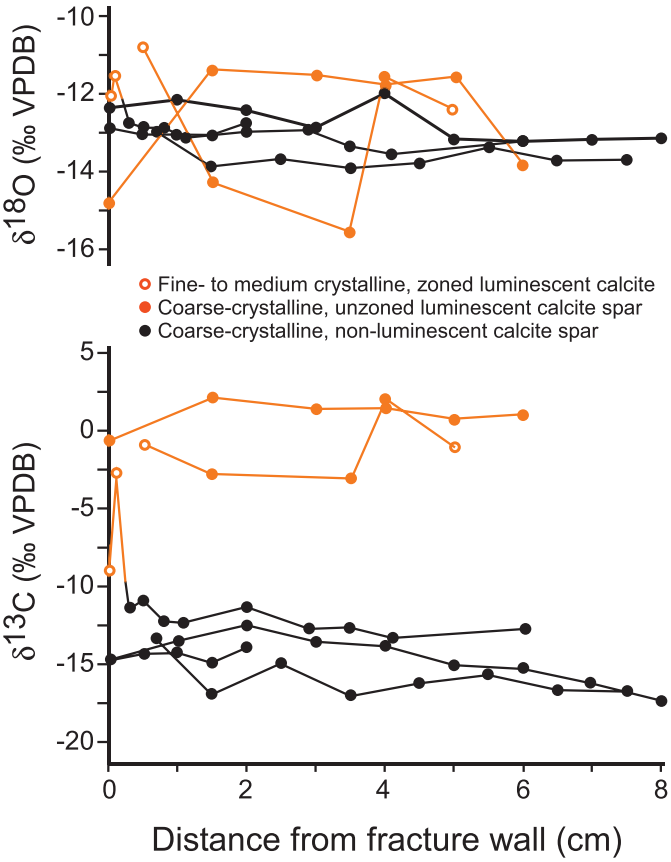

FIG. 17.—Plot of changes in oxygen and carbon stable-isotope values of calcite spars with distance from fracture walls.

than −12‰ and formed at 70°C to 96°C (average 77°C) in waters with $\delta^{18}O_{smow}$ values of −0.5 to −4.7‰ (average −3.2‰). The temperature range of both groups of coarse calcite spars overlaps with fluid-inclusion T_h values.

In fractures with more than one clumped-isotope analysis, three patterns of fracture-fill history are apparent. Some fracture fills contain components of both temperature phases, whereas others are composed of just the low-temperature phase or the high-temperature phase (Fig. 19). In all cases, temperatures of formation for the coarse calcites are greatest in the center of the fracture fill.

Geomechanical Results

Results of the geomechanical modeling (Fig. 20) indicate reactivation potential, expressed as stereonets color coded for the amount of additional pore pressure required for a fracture of any given orientation to fail. Due to considerable uncertainty in the derivation of the estimated applied stress gradients (i.e., burial depth, paleo-stress orientations, and paleo-horizontal stress magnitudes); the results provide only a relative comparison of the likelihood of structural reactivation for any given tectonic event. The greatest potential for reactivation occurred during the Permo-Triassic burial phase, with many of the syndepositional deformation features in Dark Canyon requiring no additional pore pressure to fail (Fig. 20A). Conditions were unfavorable for reactivation of high-angle (subvertical) features during the two Laramide deformation episodes (Fig. 20B, C). During Basin and Range extension, reactivation was possible as many features were close to failure (i.e., at ≤ 1 MPa of pore pressure; Fig. 20D, E). Stress conditions modeled for recent teleogenetic uplift are also possible for structural reactivation with preferential reactivation of lower-angle features most likely. Stress conditions during uplift, however, were less favorable for driving reactivation than the stresses associated with Basin and Range extension and Permo-Triassic burial.

INTERPRETATIONS

Crosscutting relations, CL characteristics, and temperatures of calcite formation collectively indicate that the diagenetic features in syndepositional fractures formed either synsedimentary, during burial, or due to teleogenetic uplift (Table 4). The geomechanical analysis ties these different diagenetic episodes to specific periods of fracture reactivation. The similarities between the authigenic phases in the fracture fill and host-limestone paragenesis also indicate that both matrix and fractures responded through time to similar episodes of fluid flow from Permian to recent time. No single fracture contains every feature described, but an idealized fill that includes all diagenetic events observed is shown in Figure 21.

Synsedimentary Events

The now-dolomitized aragonite cements in fill D and the ostracod wackestone in fill A indicated that some fractures were initially open to the seafloor. The wackestone is an inner-shelf facies and could have been infiltrated during deposition of overlying HFS deposits. Undolomitized fibrous aragonite cements intercalated with ostracod wackestone were noted in sheet cracks of Tansill shelf-crest facies in Dark Canyon by Mazzullo (1999) and were also interpreted to be marine cement and sediment, respectively.

Dolomitization of marine cements, fracturing, and precipitation of dolomite cement along some fracture walls are interpreted to be early diagenetic events. The dolomite halos adjacent to fractures time the dolomitization to post-fracturing (Melim and Scholle 1999, 2002; Koša et al. 2003). No breccia clasts were observed to be coated with dolomite cements, but some clasts are of dolomitized stratal units, thus establishing dolomitization before brecciation. The stable-isotope compositions and CL characteristics of the fracture-related dolomites are identical to dolomite in host limestones, indicating a similar origin from downward-flowing evaporated seawater during deposition of stratigraphically higher transgressive and/or highstand deposits.

The polymictic breccias are interpreted to be a karst deposit emplaced during HFS lowstands (Koša et al. 2003; Koša and Hunt 2006a). Dissolution of fracture walls (a field observation) would have been concurrent with karsting and brecciation. The CL-zoned, fine- to medium-crystalline calcite that cements the breccias, and forms the initial calcite fill in other fractures (Fig. 21), is interpreted as the product of early meteoric diagenesis. Low formation temperatures (22–32°C in outer-shelf fractures; a single value of 16°C in a platform-margin fracture) and ^{18}O-depleted parent waters (−6.2 to −10.5‰ SMOW) support the meteoric interpretation. The variation in temperatures and fluid isotopic compositions indicate multiple episodes of meteoric cementation in different syndepositional fractures at different times. This cementation was recurrent and contemporary with the syndepositional deformation and karsting, as evidenced by the fracturing, rotation, dissolution of the cements, and then regrowth of the same luminescently zoned phase (fill B). Early evaporite pseudomorphs filled by these cements (fills A, C) indicate that some calcitization of evaporites was also a synsedimentary feature. This observation means that evaporite calcitization was not limited to post-Tertiary uplift as argued by Scholle et al. (1992).

Precipitation temperatures of 16°C and 22°C for early meteoric calcite in platform-margin and outer-shelf fractures, respectively, are surprising considering the low-latitude setting and arid climate of the Permian Basin

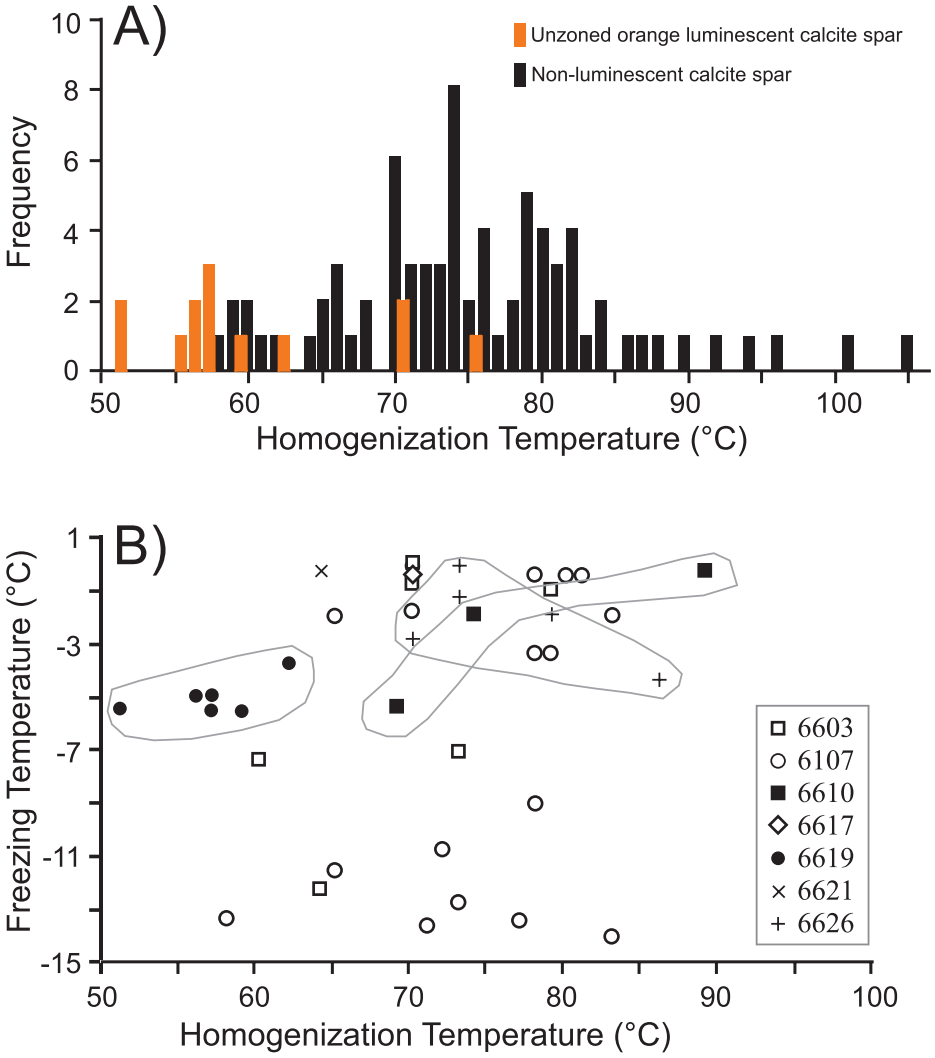

FIG. 18.—**A)** Histogram of fluid-inclusion homogenization temperatures in fracture-fill calcite spars. Data are from small (< 80 mm^2) inclusions with length-to-width ratios < 3. **B)** Plot of fluid-inclusion freezing temperature versus homogenization temperature for fracture-fill calcite spars. Decreasing freezing temperature reflects increasing fluid salinity (Goldstein and Reynolds 1994). Analyses are coded relative to fracture sample numbers (e.g., 6603, 6107, etc.) so as to illustrate the variability observed in any one fracture fill. All data are from small (< 80 mm^2) inclusions with length-to-width ratios < 3. Gray lines envelope data from the fractures that exhibit the least amount of variability in freezing temperatures (i.e., fluid salinities).

during the late Guadalupian. These temperatures and the presence of meteoric waters suggest that the paleoclimate was not always hot and arid during Tansill deposition. Far more data are needed to determine if the differences between the single platform-margin early groundwater temperature (16°C in a G30 HFS fracture) and the warmer outer-shelf groundwater temperatures (22°, 31°, and 32°C in G27 HFS fractures) reflects temporal variability in climate, spatial variability in groundwater temperatures (e.g., buffering of platform-margin meteoric groundwater by the cooler open-water mass of the adjacent basin), or some combination of both temporal and spatial factors.

Burial Events

The lack of CL zonation in the coarse-crystalline luminescent and non-luminescent calcite spars suggests they did not originate as cements, but as replacements formed as evaporites dissolved. Replacement explains the irregular patterns of inclusions, microvoids, and the CL characteristics. For example, rectilinear and lath-like CL patterns seen in both host limestones (Fig. 8F) and fractures (fill D) are compatible with replacement across thin films that preserved the anhydrite crystal structure. The highly irregular and mottled CL characteristics of other coarse calcites (fill E) also argue for a process other than growth of pore-filling cement. The microvoids, which may be partially cemented remnants of dissolved evaporite inclusions, suggest calcite replacements engulfing evaporites. Only the orange luminescent calcite that heals some microvoids (fills C, D, E) within the coarse-crystalline late spars, and grew as a zoned cement overgrowth on the coarse-crystalline spars in the center of fill E, is interpreted to be a calcite cement formed after all evaporite minerals were removed from the rocks.

Because the coarse-crystalline calcite spars are now the dominant phase in most fractures (Figs. 4, 13, 14, 21), the evaporite cements that preceded them must have once dominated the fracture fills. Evaporites did form syndepositionally as evaporites are replaced by the early meteoric calcites (fills A, C). However, some and perhaps most evaporites probably formed during Permian burial when syndepositional fractures were mostly likely to be reactivated (Fig. 20) and the overlying strata were dominated by marine evaporite-rich deposits of the Salado Formation. Downward refluxing of evaporated seawater brines from those deposits would have found the reopened fractures to be high-permeability conduits through the outer-shelf limestones. Assessing the relative abundance of evaporites formed during Tansill deposition and those formed during initial burial from later Permian brines is not possible in outcrop samples where no evaporites remain. Analysis of $^{87}Sr/^{86}Sr$ in the evaporite cements in subsurface equivalent rocks (Garber et al. 1989) might provide insights as the Sr isotope ratio of seawater has varied through time.

The clumped-isotope results indicate that the inclusion- and microvoid-rich calcites that replaced evaporites formed at relatively high temperatures (59–96°C), which is compatible with fluid-inclusion homogenization

TABLE 3.—*Results of clumped-isotope thermometry.*

Sample[1]	Luminescence[2]	$\delta^{13}C$ (‰ VPDB)	$\delta^{18}O$ (‰ VPDB)	Δ_{47} (‰)	1σ (‰)	T(Δ_{47}) (°C)[3]	1σ (°C)	$\delta^{18}O_{WATER}$ (‰ SMOW)[4]	1σ (‰)
Syndepositional fracture fills in outer-shelf facies									
6107-A	zoned orange	−8.4	−11.4	0.644	0.007	22	2	−9.7	0.5
6107-F	non	−12.3	−12.8	0.527	0.021	70	11	−2.6	1.6
6107-F rep	non	−12.3	−12.8	0.530	0.012	68	6	−2.9	0.8
6107-I	non	−12.6	−14.4	0.519	0.010	74	5	−3.6	0.7
6610-A	non	−15.4	−15.3	0.520	0.010	73	5	−4.6	0.7
6610-C	non	−14.5	−13.0	0.525	0.005	71	2	−2.6	0.4
6610-Crep	non	−14.5	−13.1	0.547	0.006	60	3	−4.4	0.4
6610-E	non	−14.7	−15.1	0.478	0.009	96	5	−1.2	0.7
6617-A	unzoned orange	−0.6	−15.8	0.506	0.009	81	5	−4.0	0.7
6617-E	unzoned orange	1.0	−13.9	0.506	0.009	81	5	−2.1	0.6
6619-A	zoned orange	0.1	−9.9	0.618	0.014	32	5	−6.2	1.0
6619-C	zoned orange	−1.8	−14.0	0.620	0.010	31	4	−10.5	0.8
6626-C	non	−14.4	−14.9	0.527	0.009	70	4	−4.7	0.7
6626-E	non	−16.9	−15.3	0.516	0.008	75	4	−4.3	0.6
6626-G	non	−16.8	−15.5	0.511	0.008	78	4	−4.1	0.6
6626-I	non	−17.1	−13.6	0.489	0.009	90	5	−0.5	0.7
Syndepositional fracture fills in reef facies									
6602-A	zoned orange	0.7	−8.8	0.662	0.009	16	3	−8.3	0.5
6602-D	unzoned orange	1.0	−11.9	0.537	0.011	65	5	−2.4	0.8
6602-D rep	unzoned orange	0.9	−12.0	0.536	0.013	65	6	−2.5	1.0
6603-F	unzoned orange	−5.4	−12.3	0.549	0.012	59	6	−3.8	0.9
6603-F rep	unzoned orange	−5.7	−12.3	0.547	0.009	60	4	−3.6	0.7

[1] Numbers denote different fractures; letters denote proximity to fracture wall (A is closest); rep = replicate.
[2] Zoned orange luminescence occurs in fine- to medium crystalline early calcite cements; unzoned orange and non-luminescence occurs in coarse-crystalline calcite.
[3] Temperature calculated from measured Δ_{47} using the theoretical thermometer calibration of Guo et al. (2009).
[4] Calculated from T(Δ_{47}) and $\delta^{18}O$ value of calcite using the calcite-water oxygen isotope fractionation relation of Kim and O'Neil (1997).

temperatures. Assuming a surface temperature of 32°C (warmest meteoric cement) and a geothermal gradient of 20°C/km, the paleotemperature data indicate burial depths of 1.3 to 3.1 km. Yet the uppermost Tansill strata in the outcrop belt were not buried below ~ 600 m (Crysdale 1987; Hill 1996). Thus, the parent fluids for the late calcite spars must have been warm waters moving upwards from deeper strata. Hill's (1996) compilation of $\delta^{18}O$ values for groundwater in the region shows that modern meteoric waters are typically −7 to −8‰ SMOW, oil-field brines are typically +2 to +4‰ SMOW, and brines associated with the Upper Permian Castile and Salado evaporites are +9 to +11‰ SMOW. These data suggest the ^{18}O depletion in the parent fluids of the fracture-fill calcite spars (−0.5 to −4.7‰ SMOW) reflects a meteoric influence, but

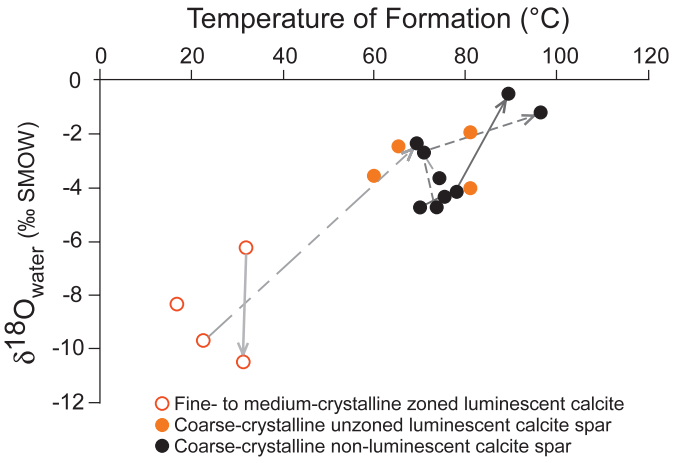

FIG. 19.—Formation temperatures of fracture-fill calcites from Δ_{47} values (T(Δ_{47})) versus parent-fluid isotopic compositions (Table 3). Dashed and solid gray lines connect successive samples from the same syndepositional fracture.

not a purely meteoric origin. Meteoric fluids, probably sourced from the southwest (McNeal 1965), circulated into the basin, mixed with hot ^{18}O-enriched brines, and then discharged upwards through the syndepositional fracture systems. Variations in the amount of mixing would explain the small range of parent-fluid $\delta^{18}O$ values and the large range of fluid salinities (Fig. 18B) recorded in the fluid-inclusion data.

The consistency of the coarse-crystalline calcites' stable-isotope values over distances of many centimeters across the fracture fills (Fig. 17) and the relatively uniform formation temperatures of those spars in any one fracture (Table 3), suggests a single flux of warm fluid calcitized the evaporites in any one fracture. Yet the coarse spars in different fractures have different $\delta^{18}O$ values and precipitation temperatures, meaning that not all fractures were calcified from exactly the same pore fluids. Fractures in the platform-margin facies in particular were calcitized at lower temperatures (60–65°C, average 63°C) than fractures in the outer-shelf facies tract (70–96°C, average 78°C). The difference in temperatures and spar $\delta^{18}O$ values are interpreted to reflect the tapping of waters from different depths in the basin. The Tansill platform-margin fractures are not associated with any fault systems (Frost et al. 2012), but the outer-shelf fractures are proximal to syndepositional faults (Fig. 3). The syndepositional faults transmitted warmer fluids upward into the outer-shelf fractures, whereas the platform-margin fractures tapped shallower, cooler fluids. Frost et al. (2012) argued that the Tansill platform margin lacks faults because of its low progradation to aggradation ratio (P/A = 3.3, Tinker 1998). In contrast the syndeformational faults in the outer-shelf facies resulted from the upward propagation of older faults in the underlying, highly progradational (P/A = 24, Kerans and Tinker 1999) Yates platform margin (Frost et al. 2012).

The extremely negative (< −9‰ VPDB; median = −13.9‰) $\delta^{13}C$ values of the non-luminescent late calcite spars are below the range of calcites formed from soil-zone-derived CO_2. Those highly negative values imply microbial degradation of ^{12}C-rich hydrocarbons (Wiggins et al. 1993) with no subsequent buffering of the carbon reservoir from

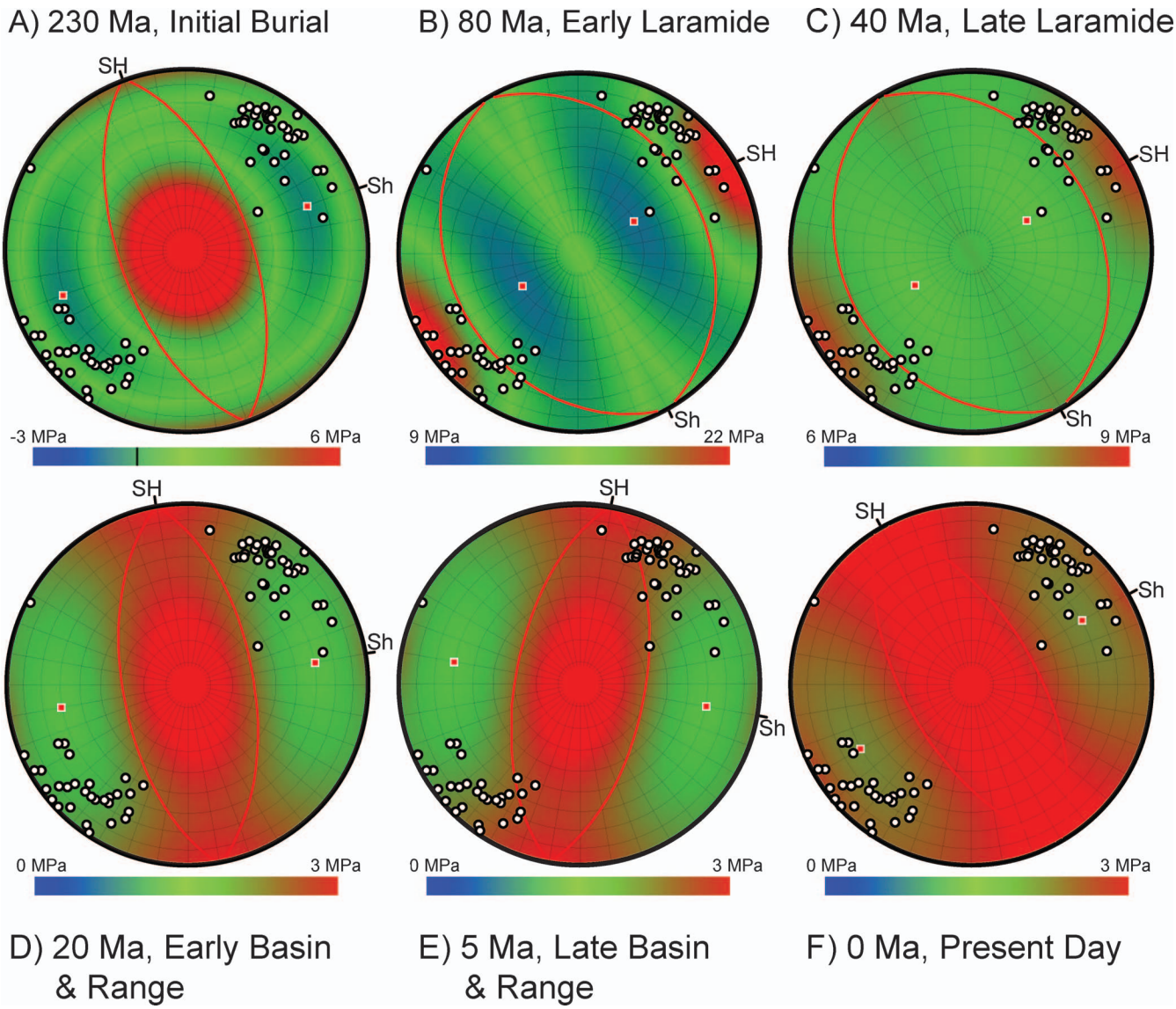

FIG. 20.—Stereonets of reactivation potential for major postdepositional deformation episodes that influenced the study area. Color coding indicates amount of additional pore pressure required for a fracture of any given orientation to fail under the assumed stress field of each time step (Table 1). Observed syndepositional fracture orientations are represented as poles (small white circles) on each plot. Slip is most likely when the additional pore pressure necessary to cause failure along a fractures is negative (i.e., $\Delta Pp \leq 0$). Red poles and red great circles represent optimal fracture orientations for frictional failure. SH = maximum horizontal stress; Sh = minimum horizontal stress.

rock–water interaction. In contrast, the orange luminescent late calcite spars (+2 to −9‰ VPDB; median = +0.3‰) are dominated by $\delta^{13}C$ values greater than −1‰, which argues for extensive rock buffering of the carbon signal and minimal ^{12}C in the parent fluids of those calcites. The ^{12}C present need not have been hydrocarbon derived either; it may have been soil-zone derived and associated with the meteoric component of the waters. Thus, although the temperatures and fluids that formed the luminescent calcite spars are the same as for the non-luminescent calcite spar, the distinctly different carbon isotope signatures mean that the parent fluids of non-luminescent spars experienced significant biodegradation of hydrocarbons before moving upwards through the fracture systems, whereas the parent fluids of the luminescent spars witnessed little, if any, oil degradation before they moved upwards.

The geomechanical modeling suggests that upward-moving warm basinal fluids were most likely to have driven evaporite replacement and formation of the luminescent and non-luminescent coarse calcites during Permo-Triassic burial or Basin and Range extension. Permo-Triassic burial, however, was unlikely to be associated with meteoric flushing of the basin inasmuch as the overlying latest Permian strata were dominated by marine-evaporite-rich deposits (i.e., Salado Formation). Basin and Range extension is thus the most likely event that drove the expulsion of the warm waters from the basin through the reactivated syndepositional fractures. Dissolution of evaporite minerals that had survived early meteoric alteration or had formed during Late Permian burial would have put Ca ions in the pore waters and driven calcite precipitation by a common-ion effect. Some fractures received warm basinal fluids that had experienced biodegradation of hydrocarbons, and were perhaps somewhat oxidizing, and thus very ^{12}C-depleted and non-luminescent (no Fe or Mn) calcites formed. Other fractures received fluids that had not experienced biodegradation of hydrocarbons and were reducing, thus they produced orange-luminescent calcites (Mn-bearing) with far less negative $\delta^{13}C$ values. Very late Basin and Range extension reactivated

TABLE 4.—*Fracture-fill paragenesis. Timing and associations with fluid types and fracture reactivation history based on interpretations presented herein.*

Syndepositional.—Concurrent with deformation and deposition of overlying high-frequency sequences. Alterations driven by fluxes of seawater, evaporated seawater, or meteoric fluids.

- Infiltration of marine sediment (Fig. 10).
- Precipitation of marine cement along fracture wall (Fig. 13).
- Dolomitization of fracture walls (fill B), infiltrated sediment, and marine cement (Fig. 13).
- Precipitation of evaporite minerals (Figs. 10, 12).
- Emplacement of karst breccia along fracture walls (Fig. 12)
- Precipitation of luminescently zoned fine- and medium-crystalline calcite cement (Figs. 10–14). Minor amount of this calcite replaced evaporites (Figs. 10, 12).
- Corrosion (Figs. 10–12) and fracturing (Fig. 11) of the luminescently zoned calcite cement with subsequent healing of fractures and corrosion surfaces by more of the same cement (Fig. 11).

Early burial.—During deposition of overlying Salado Formation. Alteration driven by refluxing evaporite brines.

- Precipitation of evaporite minerals in all open void space

Basin and Range extension.—Tectonism reactivates fractures. Alterations driven by warm waters flushed from adjacent basin.

- Replacement of anhydrite by coarse-crystalline calcite (inclusion- and microvoid-rich, unzoned orange luminescence (Fig. 12), non-luminescent (Figs. 11–14), or irregularly CL-zoned (Fig. 14). Dominant phase in most, but not all fractures.
- Microfracturing of coarse-crystalline calcite (Fig. 17).
- Precipitation of orange luminescent calcite cement that heals microvoids and microfractures and forms minor amount of luminescently zoned cement in center of fracture fills (Fig. 14).

Teleogentic overprints (formed by fracture reactivation in current stress field).

- Dissolution of calcites in center of fractures (Fig. 10, 14).
- Precipitation of laminated calcite cement (Fig. 10, 14).

fractures again, formed the microfractures that crosscut coarse-crystalline calcites and yielded the minor amounts of luminescently zoned calcite that heals microvoids and microfractures, and grew as cement overgrowths in the center of fractures (Fig. 21).

Teleogenetic Events

The final diagenetic events in the fracture-fill paragenesis, dissolution, and formation of laminated micritic and fine-crystalline calcite cements (Fig. 21), are interpreted to be related to teleogenetic uplift, karsting, and relatively recent weathering of the fracture fills. This is compatible with the geomechanical analyses that indicate that reactivation is possible in the current stress field. The dissolution was, in some cases, extensive enough to generate macroscale dissolution vugs and small caves. The micritic and very fine-crystalline calcite cements thus are interpreted to be a speleogenetic phase within those vugs. These are the same teleogenetic products that occur in the host limestones (Fig. 9E).

DISCUSSION

Two aspects of this study have broad significance. The first is with respect to the question: can syndepositional deformation features in

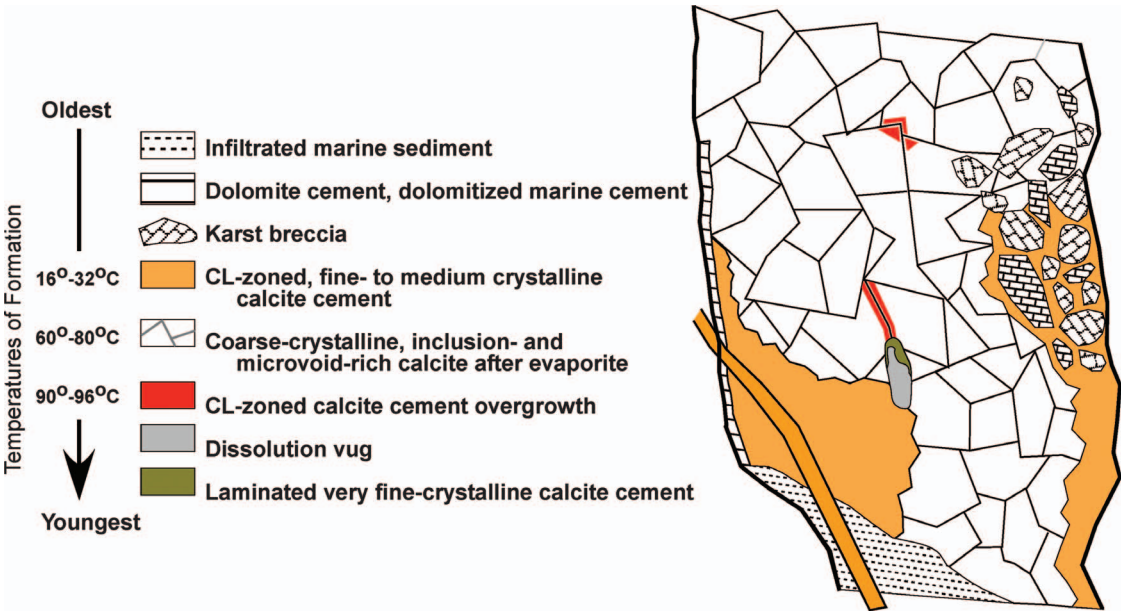

FIG. 21.—Generalized schematic of fracture fills. Diagram depicts all features observed in the fractures (Table 4), except for microscopic-scale dissolution events within cement types and evaporite phases that have been replaced by calcite. No one fracture actually contains all features. The asymmetry between fills on one wall versus the other is done to illustrate the variety of early diagenetic relations; no single fracture studied exhibited that much variability between or along its walls. Temperatures of formation are from Table 3.

platform-margin carbonates act as fluid conduits throughout the entire history of the strata? The analysis of the fracture fills in the Tansill outer-shelf carbonates shows that the answer to that question is yes. The syndepositional features in Dark Canyon formed a fluid-flow network that provided important migration pathways for numerous diagenetic fluids throughout the history of the rocks. First, there was the downward migration of meteoric fluids and seawater-derived brines during the original Tansill-age deformation. Then at least four episodes of reactivation are indicated by the paragenesis and supported by the geomechanical analyses. During Permo-Triassic burial, reactivation probably provided pathways for refluxing evaporite brines that led to extensive evaporite cementation of the fractures. Early Basin and Range extension drove evaporite calcitization and produced the high-temperature, ^{18}O-depleted spars. Late Basin and Range reactivation caused micro fractures to develop in those spars and the subsequent precipitation of calcite that resealed those micro fractures, healed microvoids in the calcite spars, and formed the hottest calcite cement in the fracture-fill centers. Lastly, the present-day stress field promoted the most recent reactivation event that drove dissolution and precipitation of a minor amount of speleogenetic calcite.

That syndepositional deformation features can reactivate throughout the history of a rock, as demonstrated herein, suggests that reactivation also might have occurred in carbonate platform margins of other settings and geologic age. The prerequisites are merely an early-cemented margin prone to syndepositional fracturing (Frost and Kerans 2010) and later stress fields that favor the reopening of those fractures. Once the syndepositional deformation network is in place, it will be preferentially reused under favorable stress orientations. Subsequent reopenings create flow paths for subsurface fluids to move vertically through the rocks and drive renewed diagenesis. For example, Jones and Xiao (2006) modeled free geothermal convection with burial in the Carboniferous Tengiz platform, and included elevated vertical flow velocities in the platform-margin carbonates to simulate open syndepositional fractures. Their results show enhanced calcite dissolution and cementation in the rising and falling limbs, respectively, of convection cells formed by vertical flow through the fractures. Their model results are supported by the presence of solution-enhanced syndepositional fractures in the Tengiz margin (Collins et al. 2006). Tinker et al. (2000) and Tinker et al. (2004) also discussed a Pennsylvanian shelf margin in which early structural features controlled sedimentation patterns, and the same features were subsequently conduits for dolomitizing hydrothermal fluids. Reactivations of syndepositional deformation features in an ancient carbonate platform have also been shown to influence drainage patterns on a modern landscape (Koša and Hunt 2006b) and localize younger karst bodies (Hurley 1986; Playford 2002). Since the scope of syndepositional deformation on carbonate platforms is only now being appreciated, further structural and diagenetic analyses such as the one presented here are required to fully appreciate the potential diagenetic impacts of reactivation.

The second aspect of this study with broad significance is the illustration of how clumped-isotope thermometry can resolve diagenetic uncertainties (e.g., Huntington et al. 2011; Ferry et al. 2011). Scholle et al. (1992) were the first to suggest that coarse-crystalline calcite replaced evaporite cements that were once widespread in the limestones of the entire late Guadalupian carbonate platform. Hill (1996), however, questioned the replacement origin of those calcite spars and whether evaporite cements were as widespread in the modern outcrop belt as envisioned by Scholle et al. (1992). The fundamental issue was how to interpret the oxygen isotope values of the coarse-crystalline calcites without constraints on temperatures of formation or the isotopic composition of the parent fluids. Mruk (1985, 1989) and Given and Lohmann (1986) argued for warm Permian meteoric groundwater, whereas Scholle et al. (1992) argued for low-temperature, ^{18}O-depleted meteoric water flushing from west to east in association with Tertiary uplift. In contrast, Hill (1996) concluded that the very negative δ^{18}O values of the calcite spars indicated a thermal event, which she suggested was Miocene in age, and that the coarse-crystalline calcites in fractures, faults, and spar caves had to be cements and could not have formed after early evaporites.

The data presented herein resolve this controversy. It is now known that the faults originated by syndepositional deformation and many of the small spar caves were karst features developed along those early deformation features (Hunt and Fitchen 1999; Hunt et al. 2002; Koša et al. 2003; Koša and Hunt 2005, 2006a). Thus the fractures and small caves were present and open during Permo-Triassic reactivation when evaporites could have formed, with the evaporite crystal forms seen in CL patterns of the calcite spar documenting that evaporites were once in those fractures. The presence of many microvoid and other irregular CL patterns in fracture-fill calcites also argue for an origin other than passive pore-filling cement. The data are compatible with Scholle et al. 's (1992) argument that evaporite minerals were once pervasive in the late Guadalupian limestones. The clumped-isotope data, however, constrain both temperatures of formation and the isotopic compositions of the parent fluids. Those data show that the "late" calcite spars in fracture fills, and by inference the host limestones, did not form in Tertiary low-temperature meteoric waters. Rather, some evaporite calcitization occurred at low temperatures in isotopic equilibrium with Permian meteoric fluids, but most of the calcite replacing evaporites formed as warm waters flushed upward with Basin and Range extension.

Dark Canyon, with its northeast-facing platform margin (Fig. 1), is oriented subparallel to many of the major Basin and Range structural features observed in the Guadalupe Mountains, such as the Huapache monocline and western-escarpment normal faults. As a result, the margin-parallel syndepositional deformation features in Dark Canyon are in a favorable orientation for reactivation by remote stresses associated with Basin and Range extension. To the south, the Capitan reef trend faces southeast and margin-parallel syndepositional deformation features are oriented orthogonal to regional Basin and Range features (Koša and Hunt 2006a). Thus, reactivation and formation of calcite spars in syndepositional fractures along the southeast-facing Capitan margin might have a different paragenetic history than those in Dark Canyon. Indeed, data from Koša and Hunt (2006a) indicate that the coarse-crystalline calcite fills observed in Dark Canyon are not volumetrically significant in the margin-parallel faults and fractures in Slaughter Canyon. Instead, calcite spar fracture fills in Slaughter Canyon are more prevalent in NW–SE-striking features that run parallel to the axis of the canyon and the Huapache Monocline (field observations by E.L. Frost). This presents an interesting hypothesis to be tested with further research: can reactivation and fracture-controlled paragenesis be predicted by analyzing the orientation of the platform-margin trend relative to regional tectonic deformation events?

CONCLUSIONS

Closely spaced syndepositional faults and fractures cut Permian (Tansill Formation) shelf-crest and outer-shelf facies in Dark Canyon, New Mexico. The paragenesis defined by petrography and isotope geochemistry indicates that the diagenetic fills in the Tansill-age syndepositional fractures are multigenerational and representative of numerous fracture openings, fills, and reactivation over their entire ~ 260 Ma history. Dolomite and calcite cements on the margins of the fractures and calcite cementing breccias in the fractures are as young as the syndepositional deformation features themselves. However, the coarse-crystalline calcite spars that dominate fracture fills originated as replacements of originally evaporite cements. Clumped-isotope data indicate that those calcites formed during a thermal (ranging from 60 to

96°C) event in which isotopically mixed waters (part meteoric, part oil-field brine) moved up and out of the adjacent Delaware Basin. Geomechanical modeling indicates that the NW–SE-oriented syndepositional fractures in Dark Canyon were most likely reactivated during Permo-Triassic burial and Miocene Basin and Range extension. The older reactivation is interpreted to have facilitated extensive evaporite cementation, whereas the second reactivation, during the thermal pulse, constrains the timing of evaporite replacement by coarse-crystalline calcite spars. The diagenetic features in the syndepositional fractures are identical to those observed in the outer-shelf limestones, suggesting that both matrix and fractures responded through time to similar episodes of fluid flow.

The results are broadly applicable in that they suggest that once a syndepositional fluid-flow network is developed in a carbonate platform, it can be reactivated and used by younger diagenetic and fluid-flow events. Since syndepositional deformation on carbonate platforms is only now being fully appreciated, further studies such as the one presented herein are going to be needed to understand the full scope of diagenetic impacts from syndepositional fracture reactivation.

ACKNOWLEDGMENTS

Supplemental data tables are available at http://sepm.org/pages.aspx?pageid=229. Zachery Wenz performed the fluid-inclusion analyses. Charles Kerans, Steve Bachtel, and Eric Hiemstra assisted in the field. ConocoPhillips Subsurface Technology provided funding for field and analytical work. We thank John Eiler for access to California Institute for Technology's clumped-isotope analytical facilities and Nami Kitchen for laboratory assistance. Reviewers Paul (Mitch) Harris, Lynn Soreghan, Leslie Melim, and Gene Rankey are thanked for their suggestions and comments. Acknowledgment is made by KWH to the donors of the American Chemical Society Petroleum Research Fund for support of this research (ACS-PRF grant 49709).

REFERENCES

Babcock, J.A., 1977, Calcareous algae, organic boundstones, and the genesis of the Upper Capitan Limestone (Permian, Guadalupian), Guadalupe Mountains, west Texas and New Mexico, *in* Hileman, M.E., and Mazzullo, S.J., eds., Upper Guadalupian Facies, Permian Reef Complex, Guadalupe Mountains, New Mexico and West Texas: SEPM, Permian Basin Section, Field Conference Guidebook, Publication 77-16, p. 3–44.

Babcock, J.A., and Yurewicz, D.A., 1989, The massive facies of the Capitan Limestone, Guadalupe Mountains, Texas and New Mexico, *in* Harris, P.M., and Grover, G.A., eds., Subsurface and Outcrop Examination of the Capitan Shelf Margin, Northern Delaware Basin: SEPM, Core Workshop 13, p. 365–372.

Byerlee, J., 1978, Friction of rock: Pure and Applied Geophysics, v. 116, p. 615–626.

Collins, J.F., Kenter, J.A.M., Harris, P.M., Kuanysheva, G., Fischer, D.J., and Steffen, K.L., 2006, Facies and reservoir-quality variations in the Late Visean to Bashkirian outer platform, rim, and flank of the Tengiz Buildup, Precaspian Basin, Kazakhstan, *in* Harris, P.M., and Weber, L.J., eds., Giant Hydrocarbon Reservoirs of the World: From Rocks to Reservoir Characterization and Modeling: American Association of Petroleum Geologists, Memoir 88, p. 55–95.

Crysdale, B.L., 1987, Fluid inclusion evidence for the origin, diagenesis and thermal history of sparry calcite cement in the Capitan Limestones, McKittrick Canyon, West Texas [unpublished MS thesis]: University of Colorado, Boulder, CO, 78 p.

Dennis, K.J., and Schrag, D.P., 2010, Clumped isotope thermometry of carbonatites as an indicator of diagenetic alteration: Geochemica et Cosmochimica Acta, v. 74, p. 4110–4122.

Dunham, R.J., 1972, Capitan Reef, New Mexico and Texas: Facts and Questions to Aid Interpretation and Group Discussion: SEPM, Permian Basin Section, Publication 72-14, 291 p.

Eiler, J.M., 2007, "Clumped-isotope" geochemistry—the study of naturally-occurring multiply-substituted isotopologues: Earth and Planetary Science Letters, v. 262, p. 309–327.

Eiler, J.M., and Schauble, E., 2004, $^{18}O^{13}C^{16}O$ in Earth's atmosphere: Geochemica et Cosmochimica Acta, v. 68, p. 4767–4777.

Esteban, M., and Pray, L.C., 1977, Origin of the pisolite facies of the shelf crest, *in* Hileman, M.E., and Mazzullo, S.J., eds., Upper Guadalupian Facies, Permian Reef Complex, Guadalupe Mountains, New Mexico and West Texas: SEPM, Permian Basin Section, Field Conference Guidebook, Publication 77-16, p. 479–486.

Esteban, M., and Pray, L.C., 1983, Pisoids and pisolite facies (Permian), Guadalupe Mountains, New Mexico and west Texas, *in* Peryt, T.M., ed., Coated Grain: Berlin, Springer-Verlag, p. 503–537.

Ferrill, D.A., Winterle, J., Wittmeyer, G., Simms, D., Colton, S., Armstrong, A., and Morris, A.P., 1999, Stressed rock strains groundwater at Yucca Mountain, Nevada: GSA Today, v. 9, no. 5, p. 1–8.

Ferry, J.M., Passey, B.H., Vasconcelos, C., and Eiler, J.M., 2011, Formation of dolomite at 40–80 °C in the Latemar carbonate buildup, Dolomites, Italy, from clumped isotope thermometry: Geology, v. 39, p. 571–574.

Finkbeiner, T., Barton, C.A., and Zoback, M.D., 1997, Relationships among *in-situ* stress, fractures and faults, and fluid flow: Monterey Formation, Santa Maria Basin, California: American Association of Petroleum Geologists, Bulletin, v. 81, p. 1975–1999.

Folk, R.L., 1974, Petrology of Sedimentary Rocks: Austin, Texas, Hemphill Publishing Co., 182 p.

Frost, E.L., III, and Kerans, C., 2010, Controls on syndepositional fracture patterns, Devonian reef complexes, Canning Basin, Western Australia: Journal of Structural Geology, v. 32, p. 1231–1249.

Frost, E.L., III, Budd, D.A., and Kerans, C., 2012, Syndepositional deformation in a high-relief carbonate platform and its effect on early fluid-flow as revealed by dolomite patterns: Journal of Sedimentary Research, v. 82, p. 913–932.

Garber, R.A., Grover, G.A., and Harris, P.M., 1989, Geology of the Capitan shelf margin—subsurface data from the northern Delaware Basin, *in* Harris, P.M., and Grover, G.A., eds., Subsurface and Outcrop Examination of the Capitan Shelf Margin, Northern Delaware Basin: SEPM, Core Workshop 13, p. 3–272.

Given, R.K., and Lohmann, KC, 1986, Isotopic evidence for the early meteoric diagenesis of the reef facies, Permian Reef complex of West Texas and New Mexico: Journal of Sedimentary Petrology, v. 56, p. 183–193.

Ghosh, P., Adkins, J., Affek, H., Balta, B., Guo, W., Schauble, E., Schrag, D.E., and Eiler, J.M., 2006, ^{13}C–^{18}O bonds in carbonate minerals: a new kind of paleothermometer: Geochemica et Cosmochimica Acta, v. 70, p. 1439–1456.

Goldstein, R.H., and Reynolds, T.J., 1994, Systematics of Fluid Inclusions in Diagenetic Minerals: SEPM, Short Course 31, 199 p.

Guo, W., Mosenfelder, J.L., Goddard, W.A.I., and Eiler, J.M., 2009, Isotopic fractionations associated with phosphoric acid digestion of carbonate minerals: insights from first-principles theoretical modeling and clumped isotope measurements: Geochimica et Cosmochimica Acta, v. 73, p. 7203–7225.

Hennings, P.H., Allwardt, P.F., Paul, P.K., Zahm, C.K., Reid, R., Alley, H., Kirschner, R., Lee, R., and Hough, E., 2012, Relationship between fractures, fault zones, stress, and reservoir productivity in the Suban gas field, Sumatra, Indonesia: American Association Petroleum Geologists, Bulletin, v. 96, p. 753–772.

Hill, C.A., 1996, Geology of the Delaware Basin: Guadalupe, Apache, and Glass Mountains, New Mexico and West Texas: Permian Basin Section, SEPM, Publication 96-39, 480 p.

Hunt, D.W., and Fitchen, W.M., 1999, Compaction and the dynamics of carbonate-platform development: insights from the Permian Delaware and Midland basins, southeastern New Mexico and West Texas, U.S.A, *in* Harris, P.M., Saller, A.H., and Simo, J.A. eds., Advances in Carbonate Sequence Stratigraphy; Application to Reservoirs, Outcrops and Models: SEPM, Special Publication 63, p. 75–106.

Hunt, D.W., Fitchen, W.M., and Koša, E., 2002, Syndepositional deformation of the Permian Capitan reef carbonate platform, Guadalupe Mountains, New Mexico, USA: Sedimentary Geology, v. 154, p. 89–126.

Huntington, K.W., Eiler, J.M., Affek, H., Guo, W., Bonifacie, M., Yeung, L.Y., Thiagarajan, N., Passey, B., Tripati, A., Daëron, M., and Came, R.E., 2009, Methods and limitations of "clumped" CO_2 isotope (Δ_{47}) analysis by gas-source isotope-ratio mass spectrometry: Journal of Mass Spectrometry, v. 44, p. 1318–1329.

Huntington K.W., Budd, D.A., Wernicke, B.P., and Eiler, J.M., 2011, Use of clumped-isotope thermometry to constrain temperature of crystallization for diagenetic calcite: Journal of Sedimentary Research, v. 81, p. 656–669.

Hurley, N.F., 1986, Geology of the Oscar Range Devonian Reef Complex, Canning Basin, western Australia [unpublished Ph.D. thesis]: University of Michigan, Ann Arbor, MI, 269 p.

Jaeger, J.C., and Cook, N.G.W., 1979, Fundamentals of Rock Mechanics: London, Chapman and Hall, 593 p.

Jones, G.D., and Xiao, Y., 2005, Dolomitization, anhydrite cementation and porosity evolution in a reflux system: insights from reactive transport models: American Association of Petroleum Geologists, Bulletin, v. 89, p. 577–601.

Jones, G.D., and Xiao, Y., 2006, Geothermal convection in the Tengiz carbonate platform, Kazakhstan: reactive transport models of diagenesis and reservoir quality: American Association of Petroleum Geologists, Bulletin, v. 90, p. 1251–1272.

Kendall, C.G.St.C., and Warren, J., 1987, A review of the origin and setting of tepees and their associated fabrics: Sedimentology, v. 34, p. 1007–1027.

Kerans, C., and Fitchen, W.M., 1995, Sequence hierarchy and facies architecture of a carbonate-ramp system: San Andres Formation of Algerita Escarpment and western Guadalupe Mountains, West Texas and New Mexico: Bureau of Economic Geology, University of Texas, Austin, Texas, Reports of Investigation 235, 86 p.

Kerans, C., and Harris, P.M., 1993, Outer shelf and shelf crest, *in* Bebout, D.G., and Kerans, C., eds., Guide to the Permian Reef Geology Trail, McKittrick Canyon, Guadalupe Mountains National Park, West Texas: Bureau of Economic Geology, University of Texas, Austin, Texas, Guidebook 26, p. 32–43.

Kerans, C., and Tinker, S., 1999, Extrinsic stratigraphic controls on development of the Capitan reef complex, *in* Saller, A.H., Harris, P.M., Kirkland, B.L., and Mazzullo, S.J., eds., Geologic Framework of the Capitan Reef: SEPM, Special Publication 65, p. 15–36.

Kim, S.-T., and O'Neil, J.R., 1997, Equilibrium and nonequilibrium oxygen isotope effects in synthetic carbonates: Geochimica et Cosmochimica Acta, v. 61, p. 3461–3475.

Kirkland, B.L., Longacre, S.A., and Stoudt, E.L., 1993, Reef, *in* Bebout, D.G., and Kerans, C., eds., Guide to the Permian Reef Geology Trail, McKittrick Canyon, Guadalupe Mountains National Park, West Texas: Bureau of Economic Geology, University of Texas, Austin, Texas, Guidebook 26, p. 23–30.

Kirkland, B.L., Longacre, S.A., and Stoudt, E.L., 1999, The dynamic Capitan reef: an image of an ancient reef and suggestions for future research, *in* Saller, A.H., Harris, P.M., Kirkland, B.L., and Mazzullo, S.J., eds., Geologic Framework of the Capitan Reef: SEPM, Special Publication 65, p. 161–173.

Koša, E., and Hunt, D.W., 2005, Growth of syndepositional faults in carbonate strata; Upper Permian Capitan Platform, New Mexico, USA: Journal of Structural Geology, v. 27, p. 1069–1094.

Koša, E., and Hunt, D.W., 2006a, Heterogeneity in fill and properties of karst-modified syndepositional faults and fractures: Upper Permian Capitan Platform, New Mexico, U.S.A.: Journal of Sedimentary Research, v. 76, p. 131–151.

Koša, E., and Hunt, D.W., 2006b, The effect of syndepositional deformation within the Upper Permian Capitan platform on the speleogenesis and geomorphology of the Guadalupe Mountains, New Mexico, USA: Geomorphology, v. 78, p. 279–308.

Koša, E., Hunt, D., Fitchen, W.M., Bockel-Rebelle, M.-O., and Roberts, G., 2003, The heterogeneity of paleocavern systems developed along syndepositional fault zones: the Upper Permian Capitan Platform, Guadalupe Mountains, U.S.A, *in* Ahr, W.M., Harris, P.M., Morgan, W.A., and Somerville, I.D., eds., Permo-Carboniferous Carbonate Platforms and Reefs: SEPM, Special Publication 78, p. 291–322.

Lucia, F.J., 1961, Dedolomitization in the Tansill (Permian) Formation: Geological Society of America, Bulletin, v. 72, p. 1107–1110.

Mazzullo, S.J., 1999, Paleoenvironments, cyclicity, and diagenesis in the outer shelf Tansill Formation in the Carlsbad embayment (Dark Canyon), northern Guadalupe Mountains, New Mexico, *in* Saller, A.H., Harris, P.M., Kirkland, B.L., and Mazzullo, S.J., eds., Geologic Framework of the Capitan Reef: SEPM, Special Publication 65, p. 107–128.

Mazzullo, S.J., and Cys, J.M., 1977 Submarine cements in Permian boundstones and reef-associated rocks, Guadalupe Mountains, West Texas and southeastern New Mexico, *in* Hileman, M.E., and Mazzullo, S.J., eds., Upper Guadalupian Facies, Permian Reef Complex, Guadalupe Mountains, New Mexico and West Texas: Permian Basin Section, SEPM, Publication 77-16, Field Conference Guidebook, p. 151–200.

McNeal, R.P., 1965, Hydrodynamics of the Permian basin, *in* Young, A., and Galley, J.E., eds., Fluids in Subsurface Environments: American Association of Petroleum Geologists, Memoir 4, p. 308–326.

Melim, L.A., and Scholle, P.A., 1999, Diagenesis of the Capitan Formation forereef facies (Permian), West Texas and New Mexico, *in* Saller, A.H., Harris, P.M., Kirkland, B.L., and Mazzullo, S.J., eds., Geologic Framework of the Capitan Reef: SEPM, Special Publication 65, p. 193–210.

Melim, L.A., and Scholle, P.A., 2002, Dolomitization of the Capitan Formation forereef facies (Permian, west Texas and New Mexico): seepage reflux revisited: Sedimentology, v. 49, p. 1207–1227.

Morris, A.P., Ferrill, D.A., and Henderson, D.B., 1996, Slip-tendency analysis and fault reactivation: Geology, v. 24, p. 275–278.

Mruk, D.H., 1985, Cementation and dolomitization of the Capitan Limestone (Permian), McKittrick Canyon, West Texas [Unpublished MS thesis]: University of Colorado, Boulder, CO, 153 p.

Mruk, D.H., 1989, Diagenesis of the Capitan Limestone, Upper Permian, McKittrick Canyon, West Texas, *in* Harris, P.M., and Grover, G.A., eds., Subsurface and Outcrop Examination of the Capitan Shelf Margin, Northern Delaware Basin: SEPM, Core Workshop 13, p. 387–406.

Mutti, M., and Simo, J.A., 1994, Stratigraphic patterns and cycle-related diagenesis of Upper Yates Formation, Permian, Guadalupe Mountains, *in* Loucks, R.L., and Sarg, J.F., eds., Carbonate Sequence Stratigraphy—Recent Developments and Applications: American Association of Petroleum Geologists, Memoir 57, p. 515–534.

Nolen-Hoeksema, R.C., Avasthi, J.M., Pape, W.C., and El Rabaa, A.W.M., 1994, Waterflood improvement in the Permian Basin: impact of in-situ stress evaluations: Society of Petroleum Engineers, Reservoir Engineering, v. 9, p. 254–260.

Osleger, D.A., 1998, Sequence architecture and sea-level dynamics of Upper Permian shelfal facies, Guadalupe Mountains, southern New Mexico: Journal of Sedimentary Research, v. 68, p. 327–346.

Parsley, M.J., and Warren, J.K., 1989, Characterization of an Upper Guadalupian barrier-island complex from the middle and upper Tansill Formation (Permian), east Dark Canyon, Guadalupe Mountains, New Mexico, *in* Harris, P.M., and Grover, G.A., eds., Subsurface and Outcrop Examination of the Capitan Shelf Margin, Northern Delaware Basin: SEPM, Core Workshop 13, p. 279–285.

Passey, B., Levin, N.E., Cerling, T.E., Brown, F.H., and Eiler, J.M., 2010, High-temperature environments of human evolution in East Africa based on bond ordering in paleosol carbonates: National Academy of Sciences, USA, Proceedings, v. 107, p. 11,245–11,249.

Playford, P.E., 2002, Palaeokarst, pseudokarst, and sequence stratigraphy in Devonian reef complexes of the Canning Basin, Western Australia, *in* Keep, M., and Moss, S.J., eds., The Sedimentary Basins of Western Australia: Petroleum Exploration Society of Australia, v. 3, p. 763–793.

Rahnis, M.A., and Kirkland, B.L., 1999, Distribution, petrography, and geochemical characterization of radiaxial calcite and associated diagenetic events in the Capitan Formation, West Texas and New Mexico, *in* Saller, A.H., Harris, P.M., Kirkland, B.L., and Mazzullo, S.J., eds., Geologic Framework of the Capitan Reef: SEPM, Special Publication 65, p. 175–191.

Resor, P.G., and Flodin, E.A., 2010, Forward modeling synsedimentary deformation associated with a prograding steep-sloped carbonate margin: Journal of Structural Geology, v. 32, p. 1187–1200.

Rudolph, K.W., 1978, Diagenesis of back-reef carbonates: an example from the Capitan complex [unpublished MS thesis]: University of Texas at Austin, Austin, TX, 159 p.

Rush, J., and Kerans, C., 2010, Stratigraphic response across a structurally dynamic shelf: the latest Guadalupian composite sequence at Walnut Canyon, New Mexico, U.S.A.: Journal of Sedimentary Research, v. 80, p. 808–828.

Schmidt, V., 1977, Inorganic and organic reef growth and subsequent diagenesis in the Permian Capitan Reef complex, Guadalupe Mountains, Texas, New Mexico, *in* Hileman, M.E., and Mazzullo, S.J., eds., Upper Guadalupian Facies, Permian Reef Complex, Guadalupe Mountains, New Mexico and West Texas: Permian Basin Section, SEPM, Publication 77-16, Field Conference Guidebook, p. 93–131.

Scholle, P.A., Ulmer, D.S., and Melim, L.A., 1992, Late-stage calcites in the Permian Capitan Formation and its equivalents, Delaware Basin margin, west Texas and New Mexico: evidence for replacement of precursor evaporites: Sedimentology, v. 39, p. 207–234.

Sibson, R.H., 1998, Brittle failure mode plots for compressional and extensional tectonic regimes: Journal of Structural Geology, v. 20, p. 655–660.

Stanton, R.L., and Pray, L.C., 2004, Skeletal–carbonate Neptunian dikes of the Capitan reef: Permian, Guadalupe Mountains, West Texas: Journal of Sedimentary Research, v. 74, p. 805–816.

Tamagawa, T., and Pollard, D.D., 2008, Fracture permeability created by perturbed stress fields around active faults in a fractured basement reservoir: American Association of Petroleum Geologists, Bulletin, v. 92, p. 743–764.

Tinker, S.W., 1998, Shelf-to-basin facies distributions and sequence stratigraphy of a steep-rimmed carbonate margin: Capitan depositional system, McKittrick Canyon, New Mexico and Texas: Journal of Sedimentary Research, v. 68, p. 1146–1174.

Tinker, S.W., Zahm, L.C., and Kerans, C., 2000, Structural controls on shelf-margin evolution and reservoir distribution in Pennsylvanian icehouse conditions: South Dagger Draw Field, New Mexico and Big Hatchet Mountains, New Mexico: American Association of Petroleum Geologists, Search and Discovery Article #90914, American Association of Petroleum Geologists, Annual Convention, New Orleans, Louisiana. Available from http://www.searchanddiscovery.com/abstracts/html/2000/annual/abstracts/0671.htm

Tinker, S.W., Caldwell, D.M., Cox, D.M., Zahm, L.C., and Brinton, L., 2004, Integrated reservoir characterization of a carbonate ramp reservoir, South Dagger Draw field, New Mexico: seismic data are only part of the story, *in* Eberli, G.P., Masaferro, J.L., and Sarg, J.F., eds., Seismic Imaging of Carbonate Reservoirs and Systems: American Association Petroleum Geologists, Memoir 81, p. 91–105.

Toomey, D.F., and Cys, J.M., 1977, Rock/biota relationships of the Permian Tansill–Capitan facies exposed on the north side of the entrance to Dark Canyon, Guadalupe Mountains, southeastern New Mexico, *in* Hileman, M.E., and Mazzullo, S.J., eds., Upper Guadalupian Facies, Permian Reef Complex, Guadalupe Mountains, New Mexico and West Texas: Field Conference Guidebook, Permian Basin Section SEPM, Publication 77-16, p. 133–150.

Weidlich, O., and Fagerstrom, J.A., 1999, Influence of sea-level changes on development, community structure, and quantitative composition of the upper Capitan massive (Permian), Guadalupe Mountains, Texas and New Mexico, *in* Saller, A.H., Harris, P.M., Kirkland, B.L., and Mazzullo, S.J., eds., Geologic Framework of the Capitan Reef: SEPM, Special Publication 65, p. 139–160.

Wiggins, W.D., Harris, P.M., and Burruss, R.C., 1993, Geochemistry of post-uplift calcite in the Permian Basin of Texas and New Mexico: Geological Society of America, Bulletin, v. 105, p. 779–790.

Wood, R., 1999, Paleoecology of the Capitan reef, *in* Saller, A.H., Harris, P.M., Kirkland, B.L., and Mazzullo, S.J., eds., Geologic Framework of the Capitan Reef: SEPM, Special Publication 65, p. 129–137.

Wood, R.A., Dickson, J.A.D., and Kirkland-George, B., 1994, Turning the Capitan reef upside down: a new appraisal of the ecology of the Permian Capitan reef, Guadalupe Mountains, Texas and New Mexico: Palaios, v. 9, p. 422–427.

Wood, R.A., Dickson, J.A.D., and Kirkland-George, B., 1996, New observations on the ecology of the Permian Capitan reef, Texas and New Mexico: Palaeontology, v. 39, p. 733–762.

Yurewicz, D.A, 1977, The origin of the massive facies of the Lower and Middle Capitan Limestone (Permian), Guadalupe Mountains, New Mexico and west Texas, *in* Hileman, M.E., and Mazzullo, S.J., eds., Upper Guadalupian Facies, Permian Reef Complex, Guadalupe Mountains, New Mexico and West Texas: Permian Basin Section, SEPM, Publication 77-16, Field Conference Guidebook, p. 45–92.

Zoback, M.D., 2007, Reservoir Geomechanics: Cambridge, United Kingdom, Cambridge University Press, 449 p.

Received 26 November 2011; accepted 7 September 2012.